The Pennsylvania State University

The Graduate School

College of Earth and Mineral Sciences

DEVELOPMENT OF AN INTEGRATED MODEL FOR COMPACTION/WATER DRIVEN RESERVOIRS AND ITS APPLICATION TO THE J1 AND J2 SANDS AT BULLWINKLE, GREEN CANYON BLOCK 65, DEEPWATER GULF OF MEXICO

A Thesis in

Petroleum and Natural Gas Engineering

by

Kevin D. Best

Copyright 2002 Kevin D. Best

Submitted in Partial Fulfillment
of the Requirements
for the Degree of

Master of Science

May 2002

We approve the thesis of Kevin D. Best.

Date of Signature

Turgay Ertekin
Professor of Petroleum and Natural Gas Engineering
Thesis Co-Advisor

Peter B. Flemings
Associate Professor of Geosciences
Thesis Co-Advisor

Michael Adewumi
Professor of Petroleum and Natural Gas Engineering
In Charge of Graduate Programs in Petroleum and
Natural Gas Engineering

Phillip M. Halleck
Associate Professor of Petroleum and Natural Gas
Engineering

I grant The Pennsylvania State University the non-exclusive right to use this work for the University's own purposes and to make single copies of the work available to the public on a not-for-profit basis if copies are not otherwise available.

Kevin D. Best

ABSTRACT

Ten years of historical production, injection, and pressure data combined with a voluminous set of rock and fluid property data are utilized to illuminate the production induced saturation changes of the J1 and J2 sand reservoirs at Bullwinkle (Green Canyon Block 65). A compositional reservoir simulation model is constructed for history matching water, gas, and pressure behavior to evaluate the mechanisms governing these behaviors. Time-lapse seismic results (Swanston, 2001) and an independent production evaluation (Comisky, 2002) of the J1 and J2 sands are integrated as a qualitative comparison of production induced changes in 1997.

Initial fluid properties are constrained by five PVT samples extracted from the J1 and J2 sands. An analysis of the PVT sample fluid properties indicate that the J1 and J2 reservoirs are undersaturated and compositionally graded. Based on this analysis an equation of state (EoS) fluid model is constructed that describes the compositional heterogeneities in depth. This model establishes the initial fluids for simulation and is used to predict phase behavior through time.

Rock and fluid interaction properties (capillary pressure and relative permeability) are characterized and modeled based on core data and a petrophysical analysis performed by Comisky (2002). Comisky (2002) identifed six Flow Units (analogous to facies) in the J1 and J2 sands and assigned each constant rock properties. Each Flow Unit is assigned specific relative permeability and capillary pressure behavior based on the constant rock properties interpreted by Comisky (2002).

Production induced compaction effects on porosity and permeability are constrained using core data combined with a material balance approach. Core data indicate that pore compressibility initially increases and then decreases with increasing vertical effective stress. This behavior is replicated using the Fetkovich (1971) material balance approach. Porosity is calculated based on the changes in pore compressibility with vertical effective stress. Permeability is empirically related to porosity, based on core data. These porosity and permeability reductions are entered into the simulation model as functions of reservoir pressure.

A 3-D compositional simulation model is constructed for history matching the J1 and J2 reservoir production and pressure behavior. The model is geologically constrained based on work by Swanston (2001) and Comisky (2002). The dynamic rock and fluid properties are developed in this study. The historical oil production and water injection are specified with the water production rate, gas production rate and pressure behaviors simulated and compared to ten years of historical data. Initial results illustrate the need for adjustment of unconstrained properties (pore compressibility, relative permeability, sand connectivity). A history match is achieved through 1997 that is supported by a production and pressure error analysis, time lapse seismic results by Swanston (2001) and an production evaluation by Comisky (2002). The model is run in predictive mode through Sept. of 1999 and proves to be robust.

TABLE OF CONTENTS

LIST OF FIGURES vi

LIST OF TABLES xiii

ACKNOWLEDGEMENTS xviii

NOMENCLATURE xix

Chapter 1 INTRODUCTION 1

Chapter 2 CHARACTERIZATION AND MODEL OF THE COMPOSITIONAL VARIATION OF THE J1 AND J2 RB RESERVOIRS AT BULLWINKLE 6

Chapter 3 RELATIVE PERMEABILITY AND CAPILLARY PRESSURE BEHAVIOR OF THE J1 AND J2 RESERVOIRS AT BULLWINKLE 57

Chapter 4 ROCK COMPACTION EFFECTS ON POROSITY AND PERMEABILITY OF THE UNCONSOLIDATED J-SANDS AT BULLWINKLE 110

Chapter 5 HISTORY MATCH SIMULATION OF THE J1 AND J2 SANDS AT BULLWINKLE, GREEN CANYON BLOCK 65, GULF OF MEXICO 162

REFERENCES 265

APPENDIX A - PRODUCTION, INJECTION, AND PRESSURE DATA 273

APPENDIX B - FLUID REGIONS IN THE J1 AND J2 SANDS 289

APPENDIX C - DERIVATION OF PORE COMPRESSIBILITY 294

LIST OF FIGURES

1-1 Bathymetric base map showing the Bullwinkle oil field in relation to the Gulf of Mexico and the Texas, Louisiana coastline. 3

2-1 J1 sand structure map with A-1 well PVT sample location shown. 8

2-2 J2 sand structure map with 109-1, A-2-BP, A-3-BP, A-4-BP, A-5-BP well PVT sample locations shown. 9

2-3 J-sand cross-section depicting fluid sample locations by sand in depth. 10

2-4 Depth versus methane and C_{7+} mole percent for the J1 and J2 sand PVT samples. 13

2-5 J1-RB and J2-RB PVT sample compositions. 14

2-6 Depth versus bubble point pressure for J-RB PVT samples. 15

2-7 Depth versus differential test gas-oil ratio at bubble point pressure for J-RB PVT samples. 15

2-8 Depth versus oil density at bubble point pressure for J-RB PVT samples. 16

2-9 Depth versus oil viscosity at bubble point pressure for J-RB PVT samples. 16

2-10 Depth versus formation volume factor at bubble point pressure for J-RB PVT samples. 17

2-11 Depth versus oil compressibility at bubble point pressure for J-RB PVT samples. 17

2-12 Initial producing GOR and reservoir pressure versus time for the J2-RB wells. 20

2-13 Comparison of initial producing GOR and PVT sample multi-stage separator GOR, for J1-RB and J2-RB samples. 21

2-14 Procedure for fluid property modeling. 23

2-15 Depth versus bubble point pressure comparison for the tuned 13-component model. 33

2-16 Depth versus differential test GOR comparison for the tuned 13-component model. 33

2-17 Depth versus differential test formation volume factor comparison for the tuned 13-component model. 34

2-18 Depth versus differential test density comparison for the tuned 13-component model. 34

2-19 Depth versus differential test viscosity comparison for the tuned 13-component model. 35

2-20 Depth versus multi-stage separator GOR comparison for the tuned 13-component model. 35

2-21 Comparison of phase envelopes for the lumped and unlumped A-2-BP fluid models. 36

2-22 Depth versus bubble point pressure for the 5-component and 13-component models. 39

2-23 Depth versus differential test GOR for the 5-component and 13-component models. 39

2-24 Depth versus differential test formation volume factor for the 5-component and 13-component models. 40

2-25 Depth versus differential test density for the 5-component and 13-component models. 40

2-26 Depth versus differential test viscosity for the 5-component and 13-component models. 41

2-27 Depth versus multi-stage separator GOR for the 5-component and 13-component models. 41

2-28 C1A and C_{7+} pseudo-component mole fraction versus depth. 42

2-29 Depth versus producing GOR and modeled multi-stage separator GOR. 43

2-30 Depth versus producing GOR and adjusted mole fraction multi-stage separator GOR. 43

2-31 Depth versus C1A pseudo-component mole fractions with linear trend fit with a least squares regression. 46

2-32 Depth versus C2-C3 pseudo-component mole fractions with back-calculated linear trend polynomial. 46

2-33 Depth versus C4-C6 pseudo-component mole fractions with linear trend fit with a least squares regression. 47

2-34 Depth versus C_{7+} pseudo-component mole fractions with linear trend fit with a least squares regression. 47

2-35 Depth versus Hvy1 pseudo-component mole fractions with back-calculated linear trend polynomial. 48

2-36 Depth versus Hvy2 pseudo-component mole fractions with linear trend fit with a least squares regression. 48

2-37 Depth versus modeled bubble point pressure for both linear and constant mole fraction extrapolations. 52

2-38 Depth versus modeled multi-stage separator GOR for both linear and constant mole fraction extrapolations. 52

2-39 Depth versus modeled density for both linear and constant mole fraction extrapolations. 53

2-40 Depth versus modeled formation volume factor for both linear and constant mole fraction extrapolations. 53

2-41 Depth versus modeled viscosity for both linear and constant mole fraction extrapolations. 54

3-1 J1 sand Flow Unit map overlain by structure contours. 59

3-2 J2 sand Flow Unit map overlain by structure contours. 60

3-3 A-32-BP capillary pressure data for J2 sand whole core plug samples. 61

3-4 65-1-ST capillary pressure data for J2 sand whole core plug samples. 62

3-5 A-32-BP capillary pressure data for J1 sand whole core plug samples. 63

3-6 Residual oil saturation versus irreducible water saturation from end-point relative permeability core data. 73

3-7 Calculated end-point relative permeabilities for Flow Units 1, 2, and 3. 73

3-8 Comparison of mercury injection test data with end-point relative permeability data 76

3-9 Modeled oil-water relative permeability for Flow Unit 1. 79

3-10 Modeled oil-water relative permeability for Flow Unit 2. 79

3-11 Modeled oil-water relative permeability for Flow Unit 3. 80

3-12 Comparison of modeled oil-water relative permeability curves for Flow Units 1, 2, and 3. 81

3-13 Modeled gas-oil relative permeability curves for Flow Units 1, 2, and 3. 81

3-14 Comparison of modeled oil-water relative permeability using Corey's (1954), Brooks & Corey's (1964), and neural network (Silpngarmlers et al. 1996) two-phase models. 85

3-15 Modeled oil-water and gas-oil capillary pressure curves for Flow Unit 1. 90

3-16 Modeled oil-water and gas-oil capillary pressure curves for Flow Unit 2. 90

3-17 Modeled oil-water and gas-oil capillary pressure curves for Flow Unit 3. 91

3-18 Modeled oil-water and gas-oil capillary pressure curves for Flow Unit 4. 91

3-19 Modeled oil-water and gas-oil capillary pressure curves for Flow Unit 5. 92

3-20 Modeled oil-water and gas-oil capillary pressure curves for Flow Unit 6. 92

3-21 Comparison of modeled oil-water capillary pressure curves for the six Flow Units. 93

3-22 Comparison of modeled gas-oil capillary pressure curves for the six Flow Units. 93

3-23 Modeled oil-water relative permeability curves for Flow Unit 1. 97

3-24 Modeled gas-oil relative permeability curves for Flow Unit 1. 97

3-25 Modeled oil-water relative permeability curves for Flow Unit 2. 98

3-26 Modeled gas-oil relative permeability curves for Flow Unit 2. 98

3-27 Modeled oil-water relative permeability curves for Flow Unit 3. 99

3-28 Modeled gas-oil relative permeability curves for Flow Unit 3. 99

3-29 Modeled oil-water relative permeability curves for Flow Unit 4. 100

3-30 Modeled gas-oil relative permeability curves for Flow Unit 4. 100

3-31 Modeled oil-water relative permeability curves for Flow Unit 5. 101

3-32 Modeled gas-oil relative permeability curves for Flow Unit 5. 101

3-33 Modeled oil-water relative permeability curves for Flow Unit 6. 102

3-34 Modeled gas-oil relative permeability curves for Flow Unit 6. 102

3-35 Comparison of modeled oil-water relative permeability curves for the six Flow Units. 103

3-36 Comparison of modeled gas-oil relative permeability curves for the six Flow Units. 103

3-37 Corey coefficient *a* versus average residual oil saturation from core data. 104

4-1 Pressure vs. depth in the J2 sand at initial conditions 112

4-2 Pore compressibility versus vertical effective stress for the 65-1-ST whole core samples. 119

4-3 Pore compressibility versus vertical effective stress for the A-32-BP whole core samples. 119

4-4 Permeability versus porosity data from the 65-1-ST whole core samples. 120

4-5 Permeability versus porosity data from the A-32-BP whole core samples. 120

4-6 Permeability versus porosity data for Flow Units 1, 2, and 3 from the A-32-BP and 65-1-ST whole core samples. 122

4-7 Permeability-porosity relationships using the Carman-Kozeny model. 122

4-8 J-sand and Rocky sand connectivity model. 126

4-9 Schematic of Fetkovich material balance model. 126

4-10 Calculated average and instantaneous pore compressibility versus vertical effective stress and time for a material balance match of historical reservoir pressure. 131

4-11 Modeled reservoir and aquifer pressure using the Fetkovich cumulative material balance approach. 132

4-12 Modeled reservoir and aquifer pressure using the Fetkovich incremental material balance approach. 132

4-13 Modeled reservoir pressure using the Fetkovich incremental material balance approach with constant pore compressibility. 138

4-14 Modeled reservoir pressure using the Fetkovich incremental material balance approach with permeabilities in the aquifer of 500 mD and 1,500 mD. 139

4-15 Modeled reservoir pressure using the Fetkovich incremental material balance approach with widths of 5,000 ft. and 15,000 ft. 140

4-16 Modeled reservoir pressure using the Fetkovich incremental material balance approach with aquifer lengths of 25,000 ft. and 100,000 ft. 142

4-17 Cartoon depicting the differences between geo-mechanical compaction and simulation model compaction. 144

4-18 Model multipliers of porosity and permeability versus vertical effective stress. 146

4-19 Modeled porosity and permeability versus vertical effective stress using the incremental pore compressibility model. 147

4-20 Permeability versus porosity using an empirical model compared with deformation data. 150

4-21 Modeled pore compressibility versus vertical effective stress at initial conditions as established by the simulation model using a single compaction input table. 154

4-22 Simulation initialization effects on input maps of porosity and permeability using a single compaction input table. 154

4-23 J1 sand compaction table region map overlain by structure contours. 155

4-24 J2 sand compaction table region map overlain by structure contours. 156

5-1 J1 sand grid overlain by structure contours (Models 1 through 5). 164

5-2 J2 sand grid overlain by structure contours (Models 1 through 5). 165

5-3 J1 net sand (dz) map overlain by structure contours (Models 1 through 5). 166

5-4 J2 net sand (dz) map overlain by structure contours (Models 1 through 5). 167

5-5 J1 Flow Unit map overlain by structure contours (Models 1 through 5). 168

5-6 J2 Flow Unit map overlain by structure contours (Models 1 through 5). 169

5-7 Model 1 J1 initial saturation (So, Sw, Sg) map overlain by structure contours. 170

5-8 Model 1 J2 initial saturation (So, Sw, Sg) map overlain by structure contours. 171

5-9 Connectivity model for the J1 and J2 sands. 175

5-10 Model 1 production and pressure results for all wells. 184

5-11 Model 1 production and pressure for the A-3-BP production well. 185

5-12 Model 1 error calculated from Equation 5-1 using the simulated cumulative gas produced from each well through March of 1997. 186

5-13 Model 1 error calculated from Equation 5-1 using the simulated cumulative water produced from each well through March of 1997. 186

5-14 Model 1 RMS_a error associated with the simulated incremental gas produced from each well through March of 1997. 187

5-15 Model 1 RMS_a error associated with the simulated incremental water produced from each well through March of 1997. 187

5-16 Model 1 weighted average error (e_w) for simulated cumulative gas produced from each well through March of 1997. 192

5-17 Model 1 weighted average error (e_w) for simulated cumulative water produced from each well through March of 1997. 192

5-18 Model 1 RMS_w error associated with the simulated incremental gas produced from each well through March of 1997. 193

5-19 Model 1 RMS_w error associated with the simulated incremental water produced from each well through March of 1997. 193

5-20 Pore compressibility behavior versus vertical effective stress and reservoir pressure for a match in Model 2. 195

5-21 Comparison of Model 2 compaction multipliers for porosity and permeability with material balance values. 196

5-22 Model 2 results of production and pressure for all wells. 197

5-23 Comparison of Model 3 and core derived Corey oil-water and gas-oil relative permeability curves for Flow Unit 4. 203

5-24 Comparison of Model 3 and core derived Corey oil-water and gas-oil relative permeability curves for Flow Unit 5. 204

5-25 Model 3 results of production and pressure for all wells. 205

5-26 Model 3 results of production and pressure for the A-31 production well. 208

5-27 J1 sand water saturation map showing saturation changes in March of 1997. 212

5-28 J2 sand water saturation map showing saturation changes in March of 1997. 213

5-29 Model 4 results of production and pressure for all wells. 214

5-30 Model 4 J1 drained pay map and time-lapse seismic difference map showing reservoir changes in 1997 (Swanston, 2001). 216

5-31 Model 4 J2 drained pay map and time-lapse seismic difference map showing reservoir changes in 1997 (Swanston, 2001). 217

5-32 Model 4 J1 water saturation map and oil-water contact map, developed from production data, showing the location of the oil-water contact with time (Comisky, 2002). 219

5-33 Model 4 J2 water saturation map and oil-water contact map, developed from production data, showing the location of the oil-water contact with time (Comisky, 2002). 220

5-34 Dip cross-section through the J1 and J2 sands showing the movement of the oil-water contact with time (Comisky, 2002). 221

5-35 Cumulative error (e_a) comparison for gas and water production for all wells through March of 1997. 222

5-36 Incremental error (RMS_a) comparison for gas production, water production, and pressure for all wells through March of 1997. 222

5-37 Model 4 error calculated from Equation 5-1 using the simulated cumulative gas produced from each well through March of 1997. 224

5-38 Model 4 error calculated from Equation 5-1 using the simulated cumulative water produced from each well through March of 1997. 224

5-39 Model 4 RMS_a error associated with the simulated incremental gas produced from each well through March of 1997. 225

5-40 Model 4 RMS_a error associated with the simulated incremental water produced from each well through March of 1997. 225

5-41 Model 4 weighted average error (e_w) for simulated cumulative gas produced from each well through March of 1997. 229

5-42 Model 4 weighted average error (e_w) for simulated cumulative water produced from each well through March of 1997. 229

5-43 Model 4 RMS_w error associated with the simulated incremental gas produced from each well through March of 1997. 230

5-44 Model 4 RMS_w error associated with the simulated incremental water produced from each well through March of 1997. 230

5-45 Comparison of Model 3 and Model 4 results for gas production and pressure in the A-11-BP well. 231

5-46 Model 4 production and pressure for the A-4-BP and A-32-BP production wells. 232

5-47 Model 4 production and pressure for the A-38 and A-38-ST production wells. 233

5-48 Model 4 production and pressure for the A-60 production well. 234

5-49 Model 4 production and pressure for the A-31 and A-35 production wells. 235

5-50 Model 4 production and pressure for the A-37 and A-2-BP production wells. 236

5-51 Model 4 production and pressure for the A-3-BP and A-5-BP production wells. 237

5-52 Model 4 production and pressure for the A-34 and A-1 production wells. 238

5-53 Model 4 production and pressure for the A-11-BP and A-33 production wells. 239

5-54 Model 4 production and pressure for the A-41 production well. 240

5-55 Model 4 pressure for the A-9 and A-10 injection wells. 241

5-56 Model 4 pressure for the A-36 and A-39 injection wells. 242

5-57 Model 4 pressure for the A-42-ST injection well. 243

5-58 Model 4 production and pressure for all wells showing prediction results from 1997 through September of 1999. 245

5-59 Model 4 sensitivity of gas production using three different hydrocarbon compositions for the J1 and J2 RB reservoirs. 248

5-60 Model 4 sensitivity of average hydrocarbon pressure for three different aquifer sizes, 253

5-61 Model 5 production and pressure for all wells using constant rock properties. 256

5-62 Bar graph of the sum of the cumulative errors for all the sensitivity cases. 257

5-63 Bar graph of the sum of the incremental RMS_a errors for all the sensitivity cases. 257

A-1 Total production for the J1 and J2 sand reservoirs over a ten-year period. 274

A-2 Cumulative gas-oil ratio (GOR) for ten-year production period for wells in the J1 and J2 reservoirs. 274

A-3 A-3-BP gas-oil ratio (GOR) and water cut history data. 277

A-4 A-4-BP gas-oil ratio (GOR) and water cut history data. 277

A-5 A-60 gas-oil ratio (GOR) and water cut history data. 278

A-6 A-2-BP gas-oil ratio (GOR) and water cut history data. 278

A-7 A-33 gas-oil ratio (GOR) and water cut history data. 279

A-8 Bottom hole pressure measurements versus time for the J1, J2, J3, and J4 sands. 279

B-1 J1 sand equilibrium region map with structure contours overlain. 290

B-2 J2 sand equilibrium region map with structure contours overlain. 291

LIST OF TABLES

2-1 PVT sample data for J-sand reservoirs. 11

2-2 Reported PVT sample mole fractions for the J1-RB and J2-RB. 11

2-3 Reported PVT sample bubble point pressure fluid properties from differential test for the J-sand reservoirs. 11

2-4 Reported PVT sample C_{7+} properties for the J1-RB and J2-RB. 18

2-5 PVT sample multi-stage separator GOR, producing GOR and recombination GOR. 18

2-6 Constant mass expansion PVT data for the A-2-BP. 25

2-7 Differential liberation PVT data for the A-2-BP. 25

2-8 Gas differential liberation PVT data for the A-2-BP. 26

2-9 Flash liberation PVT data for the A-2-BP. 26

2-10 Multi-stage separator PVT data for the A-2-BP. 26

2-11 C_{7+} properties for the A-2-BP. 26

2-12 Derived heavy-end pseudo-component parameters for the A-2-BP. 27

2-13 Derived heavy-end C_1 binary interaction parameters. 27

2-14 13-Component Peng-Robinson EoS model for the A-2-BP. 29

2-15 Binary interaction parameters for the 13-component model. 29

2-16 Tuned 13-component EoS model for the A-2-BP. 30

2-17 Tuned binary interaction parameters for the 13-component model. 30

2-18 13-component model compositions from PVT data and derived pseudo-component compositions. 31

2-19 Reported PVT sample properties at reservoir conditions. 31

2-20 Tuned 13-component model fluid properties at reservoir conditions. 31

2-21 Lumped 5-component EoS model for the A-2-BP. 37

2-22 Lumped binary interaction parameters for the 5-component model. 37

2-23 Lumping scheme for EoS model. 37

2-24 Lumped compositions for sample wells. 37

2-25 Lumped 5-component model fluid properties at reservoir conditions. 44

2-26 Adjusted mole fraction results for producing GOR match. 44

2-27 Comparison of adjusted mole fraction multi-stage separator GOR to producing GOR. 44

2-28 Linear coefficients for the 5 pseudo-components and C_{7+} mole fractions. 49

2-29 Modeled mole fractions for linear composition extrapolation model. 49

2-30 Modeled mole fractions for constant composition extrapolation model. 50

2-31	Modeled fluid properties for the linear composition extrapolation model.	55
2-32	Modeled fluid properties for the constant composition extrapolation model.	55
3-1	Atmospheric properties of whole core samples used for mercury injection test.	64
3-2	Stressed properties of whole core samples used for mercury injection test.	64
3-3	Mercury-air, calculated oil-water and gas-oil capillary pressure data for sample 53A (Flow Unit 1).	65
3-4	Mercury-air, calculated oil-water and gas-oil capillary pressure data for sample 2 (Flow Unit 2).	66
3-5	Mercury-air, calculated oil-water and gas-oil capillary pressure data for sample 20 (Flow Unit 3).	67
3-6	Two-phase interfacial tension and contact angles.	69
3-7	End-point relative permeability test sample data at atmospheric conditions.	74
3-8	End-point relative permeability test sample data from stressed whole core samples.	82
3-9	Calculated end-point relative permeability values.	82
3-10	Average oil-water end-point saturation and relative permeabilities from whole core data for Flow Units 1, 2, and 3.	82
3-11	Modeled oil-water relative permeability for Flow Units 1, 2, and 3 from whole core data.	83
3-12	Modeled gas-oil relative permeability for Flow Units 1, 2, and 3 from whole core data.	83
3-13	Modeled oil-water relative permeability using Brooks and Corey's two-phase model (1964).	86
3-14	Modeled oil-water relative permeability using a neural network two-phase model (Silpngarmlers et al., 1996).	86
3-15	Rock properties for wells in Flow Unit 1.	94
3-16	Rock properties for wells in Flow Unit 2.	94
3-17	Rock properties for wells in Flow Unit 3.	94
3-18	Rock properties for wells in Flow Unit 4.	94
3-19	Rock properties for wells in Flow Unit 5.	95
3-20	Rock properties for wells in Flow Unit 6.	95
3-21	Average porosity and initial water saturation with estimated residual oil saturation.	95

3-22 Oil-water Corey coefficient *a* and *c* values used to model oil-water relative permeability for the six Flow Units described by Comisky (2001). 105

3-23 Modeled oil-water and gas-oil relative permeability and capillary pressure for Flow Unit 1. 106

3-24 Modeled oil-water and gas-oil relative permeability and capillary pressure for Flow Unit 2. 106

3-25 Modeled oil-water and gas-oil relative permeability and capillary pressure for Flow Unit 3. 107

3-26 Modeled oil-water and gas-oil relative permeability and capillary pressure for Flow Unit 4. 107

3-27 Modeled oil-water and gas-oil relative permeability and capillary pressure for Flow Unit 5. 108

3-28 Modeled oil-water and gas-oil relative permeability and capillary pressure for Flow Unit 6. 108

4-1 Deformation data from the 65-1-ST whole core, sample 10 located in the J2-sand. 113

4-2 Deformation data from the 65-1-ST whole core, sample 14 located in the J2-sand. 113

4-3 Deformation data from the 65-1-ST whole core, sample 22 located in the J2-sand. 114

4-4 Deformation data from the A-32-BP whole core, sample 16 located in the J1-sand. 114

4-5 Deformation data from the A-32-BP whole core, sample 19 located in the J1-sand. 115

4-6 Deformation data from the A-32-BP whole core, sample 21 located in the J1-sand. 115

4-7 Deformation data from the A-32-BP whole core, sample 33 located in the J2-sand. 115

4-8 Deformation data from the A-32-BP whole core, sample 46 located in the J2-sand. 116

4-9 Deformation data from the A-32-BP whole core, sample 51 located in the J2-sand. 116

4-10 Deformation data from the A-32-BP whole core, sample 56 located in the J2-sand. 116

4-11 Pressure vs. depth in the J2 sand at initial conditions. 117

4-12 Average rock properties from whole core samples for the three samples Flow Units (1, 2, and 3). 123

4-13 Permeability-porosity relations for three different grain sizes using the Carman-Kozeny model. 123

4-14 Input properties for the Fetkovich material balance model. 127

4-15 Reservoir and aquifer volumes for the J-sands and Rocky. 127

4-16 Derived average pore compressibility values from the cumulative Fetkovich material balance approach. 133

4-17 Derived instantaneous pore compressibility values from the incremental Fetkovich material balance approach. 134

4-18 Modeled reservoir and aquifer pressure for the calculated average pore compressibility behavior. 135

4-19 Modeled reservoir and aquifer pressure for the calculated instantaneous pore compressibility behavior. 136

4-20 Reservoir compaction effects on porosity. 148

4-21 Permeability-porosity model results for different "*m*" values 151

4-22 Empirical constant *m* value and curvature exponents for the permeability-porosity model. 151

4-23 Reservoir compaction effects on permeability. 152

4-24 J1 and J2 sand compaction regions by fluid type. 157

4-25 Simulation model compaction region input tables for compaction regions 1 and 2. 158

4-26 Simulation model compaction region input tables for compaction regions 3 and 4. 159

4-27 Simulation model compaction region input tables for compaction region 5. 160

5-1 Flow Unit constant properties. 172

5-2 Fluid contact locations for the J1 and J2 reservoirs. 172

5-3 Fluid properties for the J1 and J2 aquifers. 176

5-4 J3, J4, and Rocky sands equivalent aquifer pore volume multiplier. 176

5-5 Model 1 two-month initialization period changes in pressure, saturation, and composition. 180

5-6 Model 1 surface and sub-surface hydrocarbons in-place and recoverable hydrocarbons compared with values calculated by Comisky (2002). 182

5-7 Model 1 results of simulated total gas and water production from all wells and pressure through March of 1997. 188

5-8 Model 1 results for cumulative error (e_a, e_w) associated with simulated gas and water production for all wells through March of 1997. 189

5-9 Model 1 results for incremental error (RMS_a, RMS_w) associated with simulated gas and water production for all wells through March of 1997. 190

5-10 Model 2 developed pore compressibility values. 198

5-11 Simulation model compaction region input tables for regions 1 and 2. 199

5-12 Simulation model compaction region input tables for regions 3 and 4. 200

5-13 Simulation model compaction region input tables for region 5. 201

5-14 Model 3 developed oil-water and gas-oil relative permeability and capillary pressure data for Flow Unit 4. 206

5-15 Model 3 developed oil-water and gas-oil relative permeability and capillary pressure data for Flow Unit 5. 206

5-16 History match cumulative error (e_a) comparison of total gas and water production for all wells through March of 1997. 209

5-17 History match RMS_a error comparison of total gas and water production for all wells through March of 1997. 209

5-18 Modeled total hydrocarbons in place and recoverable hydrocarbons from the four models. 210

5-19 Model 4 results for cumulative error (e_a, e_w) associated with simulated gas and water production for all wells through March of 1997. 226

5-20 Model 4 results for incremental error (RMS_a, RMS_w) associated with simulated gas and water production for all wells through March of 1997. 227

5-21 Model 4 cumulative error (e_a) comparison of total gas and water production between March of 1997 and September of 1999. 246

5-22 Model 4 RMS_a error comparison of total gas and water production between March of 1997 and September of 1999. 246

5-23 Constant composition model mole fractions. 249

5-24 Fluid properties for the constant composition model mole fractions. 249

5-25 Model 4 cumulative error (e_a) comparison for three cases consisting of different J-RB fluid compositions. 250

5-26 Model 4 RMS_a error comparison for three cases consisting of different J-RB fluid compositions. 250

5-27 Model 4 cumulative error (e_a) comparison for three cases consisting of different aquifer sizes. 254

5-28 Model 4 RMS_a error comparison for three cases consisting of different aquifer sizes. 254

5-29 Model 4 and 5 (constant rock property model) cumulative error (e_a) comparison. 258

5-30 Model 4 and 5 (constant rock property model) RMS_a error comparison. 258

A-1 Production well data for the J1 and J2 reservoirs. 281

A-2 Production data for the J1 and J2 production wells. 282

A-3 Well data for the J1 and J2 injection wells. 283

A-4 Injection data for the J1 and J2 injection wells. 283

A-5 Total daily production volumes for the J1 and J2 reservoirs. 284

A-6 Total daily production volumes for the J1 and J2 reservoirs (Continued). 285

A-7 Total daily production volumes for the J1 and J2 reservoirs (Continued). 286

A-8 Historical pressure data, adjusted to 12070 ft., SSTVD, for wells in the J1 and J2 reservoirs. 287

A-9 Historical pressure data, adjusted to 12070 ft., SSTVD, for wells in the J1 and J2 reservoirs (Continued). 288

B-1 J1 and J2 RA reservoir mole fractions. 293

B-2 J1 and J2 RA reservoir fluid properties at the A-60 well location. 293

B-3 Southern Corridor region mole fractions. 293

ACKNOWLEDGEMENTS

The research discussed in this thesis is a part the Petroleum GeoSystems Initiative at The Pennsylvania State University, which is sponsored and supported by The Shell Foundation, Shell Exploration & Production Company, Landmark Graphics, and IBM. Shell provided all the data utilized within this research and Landmark Graphics supplied the modeling software and software support.

I wish to thank several Shell employees (Dave Miller, Tucker Burkhart, Dave Brown, Jeff Johnson, and John Kendrick) for many insightful discussions regarding all aspects of this research. I also wish to thank Jim Ashbaugh, of PennGeneral Energy, who gave countless hours of his time guiding and helping me in my first year of grad school.

I am grateful to my advisors, Turgay Ertekin and Peter Flemings, who made this program available and guided my progress throughout.

I am indebted to my fellow GeoSystems teammates, Joe Comisky and Alastair Swanston, for their intellectual insights and for all the humorous and interesting times in 20 Hosler! I also wish to thank all the Petroleum Engineering and Geoscience graduate students who made my graduate experience truly “fascinating”.

Finally, I wish to thank my parents, brother, and close friends for their support, understanding, and guidance.

NOMENCLATURE

Symbol	Description	Dimension
a	Wetting phase Corey coefficient	Dimensionless
a_{1i}	Polynomial coefficient of component i	Dimensionless
a_{2i}	Polynomial coefficient of component i	Dimensionless
b	Wetting phase Corey exponent	Dimensionless
b	Reservoir and aquifer width	L
bbl	Reservoir barrel	L^3
Bg	Gas formation volume factor	L^3/L^3
Bo	Oil Formation volume factor	L^3/L^3
Bo*	Oil Formation volume factor -adjusted to field separator conditions	L^3/L^3
Boi	Initial oil formation volume factor	L^3/ L^3
B.P.	Bubble point pressure	M/LT^2
Bt	Total formation volume factor	L^3/L^3
Bwi	Initial water formation volume factor	L^3/ L^3
c	Non-wetting phase Corey coefficient	Dimensionless
cc	Cubic centimeter	L^3
c_e	Total reservoir compressibility	L^2/M
c_o	Oil compressibility	L^2/M
c_p	Pore compressibility	L^2/M
cp	Centipoise	M/LT
c_{tw}	Total aquifer compressibility	L^2/M
c_w	Water compressibility	L^2/M
cp	Centipoise	M/LT
C	Gas-oil realitive permeability constant	Dimensionless
C.I.	Contour Interval	L
d	Non-wetting phase Corey exponent	Dimensionless
D	Grain size	L
dx	Grid block thickness	L
dy	Grid block width	L
dz	Subsurface true vertical depth	L
e	Oil relative permeability constant	Dimensionless
e_a	Simulated cumulative produced error	Dimensionless
e_w	Weighted simulated cumulative produced error	Dimensionless
ft.	Feet	L
FVF	Formation volume factor	L^3/L^3
g	Acceleration due to gravity	M/T^2
gm	Grams	M
GOR	Gas-oil ratio	L^3/L^3
H	Height above free water level	L

Symbol	Description	Dimension
h	Sand thickness	L
k	Permeability	L
k_{brine}	Absolute permeability of laboratory brine	L^2
kh	Horizontal (x, y) permeability	L^2
ko	Oil permeability in the presence of irreducible water	L^2
krog	Oil relative permeability in the presence of gas	Dimensionless
krow	Oil relative permeability in the presence of water	Dimensionless
krg	Gas relative permeability in the presence of liquid	Dimensionless
krwt	Wetting phase relative permeability in the presence of the non-wetting phase	Dimensionless
krnwt	Non-wetting phase relative permeability in the presence of the wetting phase	Dimensionless
krw	Water relative permeability in the presence of oil	Dimensionless
kv	Vertical (z) permeability	L^2
k_w	Permeability in the aquifer	L
kw	Water permeability in the presence of residual oil	L^2
l	Aquifer length	L
L	Reservoir length	L
LIQMF	Liquid mole fraction	Dimensionless
m	Empirical constant	L
MSCF/D	Thousand standard cubic feet per day	L^3/T
M.W.	Molecular weight	M
N	Original oil in place	L^3
n_i	Mole fraction of component i	Dimensionless
Np	Total monthly oil produced	L^3
OGOC	Original gas-oil contact	L
Omega A	Equation of state parameter	Dimensionless
Omega B	Equation of state parameter	Dimensionless
OOWC	Original oil-water contact	L
OWC	Oil-water contact	L
p	Reservoir pressure	M/LT^2
p_{aq}	Average aquifer pressure	M/LT^2
P.I.	Productivity Index	L^3/T
Parachor	Equation of state parameter	Dimensionless
P_c	Critical pressure	M/LT^2
Pc_{go}	Gas-oil capillary pressure	M/LT^2
Pc_{ma}	Mercury-air capillary pressure	M/LT^2
Pc_{ow}	Oil-water capillary pressure	M/LT^2
p_i	Initial reservoir pressure	M/LT^2
p_p	Pore pressure – equal to reservoir pressure	M/LT^2
p_{res}	Reservoir-aquifer interface pressure	M/LT^2
p_{sample}	Reservoir pressure at extraction date of PVT sample	M/LT^2
p_{sat}	Saturation Pressure	M/LT^2

Symbol	Description	Dimension
psi	Pounds per square-inch	M/L^2
psi-1	Square-inch per pound	L^2/M
PVMULT	Porosity multiplier	Dimensionless
qwi	Maximum aquifer flow rate	L^3/T
Res. bbl	Barrels of oil at reservoir conditions	L^3
RMS_a	Incremental error using a root-mean-square	L^3/T
RMS_w	Weighted incremental error using a root-mean-square	L^3/T
Rso	Solution gas-oil ratio	L^3/L^3
S	Spreading coefficient	M/T^2
SCF	Standard cubic feet	L^3
Sg	Gas saturation	Dimensionless
S_{Hg}	Mercury saturation	Dimensionless
S_{liq}	Liquid (oil + water) saturation	Dimensionless
So	Oil saturation	Dimensionless
Soi	Initial oil saturation	Dimensionless
Sor	Residual oil saturation	Dimensionless
SSTVD	Sub-surface true vertical depth	L
STB	Stock tank barrel	L^3
STB/D	Stock tank barrel per day	L^3/T
S_v	Overburden stress	M/L^2
Sw	Water saturation	Dimensionless
Swc	Connate water saturation	Dimensionless
Swi	Initial water saturation	Dimensionless
Swir	Irreducible wetting phase saturation	Dimensionless
Swirr	Irreducible water saturation	Dimensionless
Sw*	Effective water saturation	Dimensionless
Swt	Wetting phase saturation	Dimensionless
T	Tortuosity	Dimensionless
TAMULT	Permeability multiplier	Dimensionless
T_c	Critical temperature	K
Δt_n	Time step size	T
Vp	Pore volume	L^3
We	Encroached water	L^3
Wei	Maximum encroachable water	L^3
W_{inj}	Total monthly water injected	L^3
Wp	Total monthly water produced	L^3
V	Fluid volume	L^3
Vsat	Fluid volume at saturation pressure	L^3
w	Acentric factor	Dimensionless
x_i	Normalized mole fraction of component I	Dimensionless
z	Sub-sea true vertical depth	L
Z	Gas deviation factor	Dimensionless
Z_c	Critical gas compressibility factor	Dimensionless

Symbol	Description	Dimension
μ	Viscosity	M/LT
μ_w	Brine viscosity	M/LT
σ_{ma}	Mercury-air interfacial tension	M/T^2
σ_{new}	Non-reference vertical effective stress	M/L^2
σ_{ow}	Oil-water interfacial tension	M/T^2
σ_{go}	Gas-oil interfacial tension	M/T^2
σ_{gw}	Gas-water interfacial tension	M/T^2
σ_{ref}	Reference vertical effective stress	M/L^2
σ_v	Vertical effective stress	M/L^2
θ_{ma}	Mercury-air contact angle	Dimensionless
θ_{ow}	Oil-water contact angle	Dimensionless
ρ	Fluid density	M/L^3
ρ_w	Water density	M/L^3
ρ_o	Oil density	M/L^3
Φ	Porosity	Dimensionless

Chapter 1

INTRODUCTION

Numerical simulation of hydrocarbon reservoirs is typically performed to optimize and/ or predict the maximize hydrocarbon recovery of a modeled reservoir. This predictive tool is developed based on limited fluid, well, and core data that is characterized and modeled to mimic the static and dynamic properties under investigation. These individual models of rock and fluid properties are combined to simulate production and pressure with the quality determined based on qualitative analysis of a match to historical data. The results lead to the adjustment of the dynamic rock and fluid properties and sand connectivity such that future reservoir performance can be predicted based on the confidence of modeled historical behavior.

Reservoir simulation is a tool that gives insight into dynamic rock and fluid behavior for reserve estimation and evaluation of past and future reservoir performance (Warner et al., 1979, Harris, 1975). Mattax et al. (1990) stated that reservoir simulation might be the only reliable method to predict performance of large complex reservoirs. Additionally, simulation results, when combined with 3-D time-lapse seismic results, form a reservoir-monitoring tool for mapping changes associated with production (Landrø et al., 1999; Johnston et al., 2000) that can be used to understand past reservoir behavior for future prediction.

This study uses ten years of production, injection, and pressure data combined with PVT data, whole core data, a petrophysical analysis (Comisky, 2002), and time-lapse seismic results (Swanston, 2001) to model production induced changes in the J1 and J2 sand reservoirs, at Bullwinkle (Green Canyon Block 65) (Figure 1-1), for future assessment of hydrocarbon reserves. The study focuses on the characterization, modeling and integration of data from multiple sources (whole core, PVT, well-log) and disciplines (Geology and Geophysics) to gain insight and an understanding of the dynamic behavior of the J1 and J2 sands.

In this thesis, Chapters 2, 3, and 4 focus on the characterization and modeling of the components for reservoir simulation and Chapter 5 discusses the modeling of the total J1 and J2 system. Documented pressure communication (Holman and Robertson, 1994) and varying producing gas-oil ratios in depth (Appendix A), are supported by PVT data and are the basis for construction of a compositionally graded equation of state fluid model, which is discussed in Chapter 2. A petrophysical analysis performed by Comisky (2002) establishes six Flow Units (analogous to facies) each having constant rock properties that form the basis for the development of capillary pressure and relative permeability behavior as discussed in Chapter 3. In Chapter 4, a model for production induced rock compaction and the effects on porosity and permeability is developed. Finally, in Chapter 5 a simulation model is constructed for history matching production and pressure behavior using geophysical (Swanston, 2001) and geologic (Comisky, 2002) interpretations combined with the dynamic models developed in this thesis.

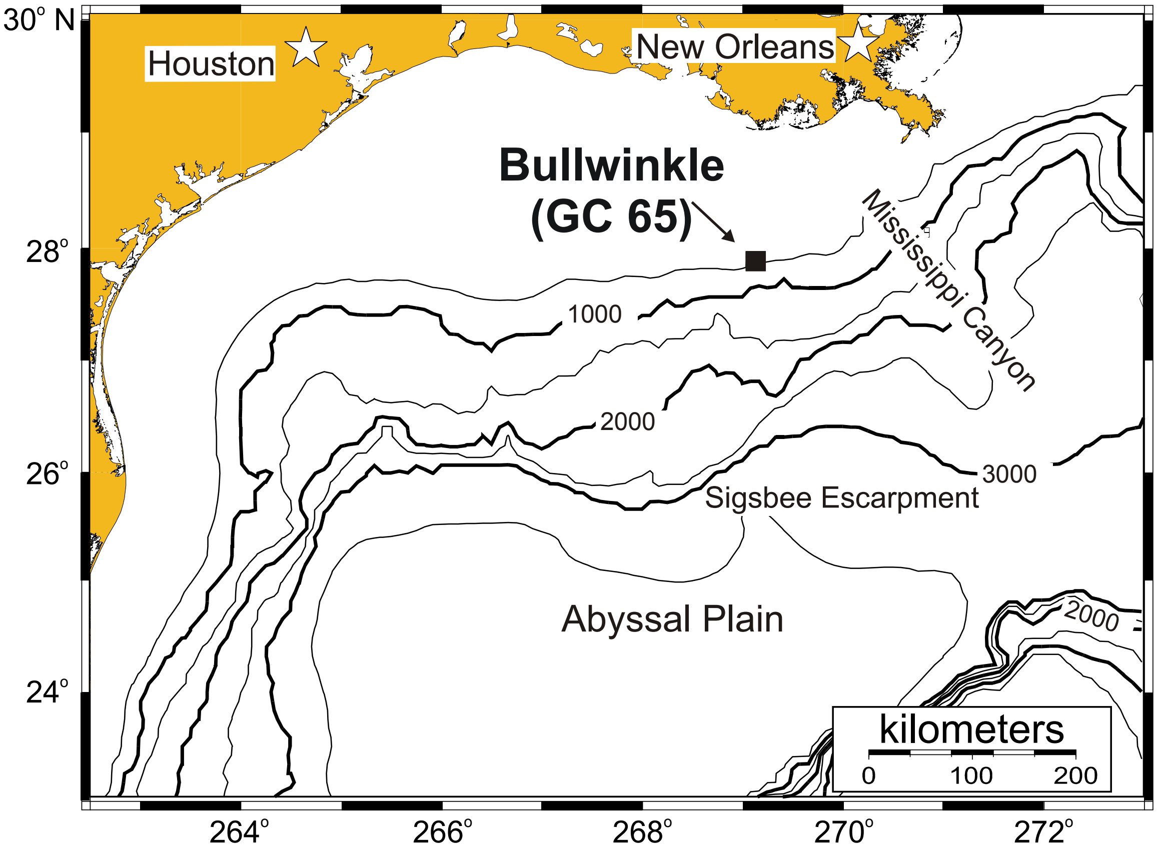
30° N
28°
26°
24°
264°
266°
268°
270°
272°
Houston
New Orleans
Bullwinkle
(GC 65)
Mississippi Canyon
1000
2000
3000
2000
Sigsbee Escarpment
Abyssal Plain
kilometers
0
100
200

Figure 1-1: Location map showing the Bullwinkle oil field in relation to the Gulf of Mexico and the Texas, Louisiana coastline. Bathymetric contours are in meters at a contour interval of 500 m. The Bullwinkle Field is located 240 km (160 miles) southwest of New Orleans in blocks 64, 65, 108, and 109 of the Green Canyon region.

BACKGROUND

Green Canyon Block 65, "Bullwinkle"

The Bullwinkle field (Green Canyon Blocks 64, 65, and 109) is a deepwater oilfield located approximately 150 miles southwest of New Orleans, Louisiana in the Gulf of Mexico (Holman et al. 1994) (Figure 1-1). Shell Offshore Inc. discovered the prospect in 1983 with initial production beginning in July of 1989 (Holman et al. 1994). A conventional fixed platform was installed in 1353 ft. of water and designed to produce 59,000 stock tank barrels of oil per day (STB/D) and 100 million standard cubic feet of gas per day (MMSCF/D) (Parjus et al., 1996). The field has produced over 130 MMBOE to date and is anticipated to produce an estimated 160 MMBOE of the estimated 260 MMBOE originally in-place. The prolific "J" sand package (J1, J2, J3, J4) contains over 90% of the field reserves (Holman et al., 1994) with approximately 70% from the J1 and J2 sands collectively.

The J-sands are interconnected sheet and channel turbidity sands of Nebraskan age (3.35 Ma) (Flemings et al., 2001). The hydrocarbon bearing reservoirs are located on the north-west flanks of a salt withdrawal minibasin and span within a vertical distance between 10600 ft to 12415 ft subsurface true vertical depth (SSTVD). Rock properties are of high quality with core porosities ranging from 29% to 33% and permeabilities of several darcies (Comisky, 2002). The hydrocarbon fluids of the J-sand reservoirs are mostly undersaturated oil, having API gravities ranging from 30^{o} to 27^{o} over a vertical column height of 1400 ft (Westrich et al. 1999). These rock and fluid properties combined with exceptionally high pore compressibilities (10E-6 to 80E-6 psi-1)

(Flemings et al., 2001) and a well-connected aquifer make the J-sands a compaction drive/ water drive system.

The focus of this study is on the J1 and J2 sands, which contain the largest volume of hydrocarbons within the J-sands and within the Bullwinkle minbasin. These sands average between 30 and 100 ft. in thickness with the J1 located vertically above the J2 separated by 0-50 ft. of shale. The J1 sand has well defined seismic boundaries, while the J2 aquifer was mapped to the southern boarder of the seismic survey (Swanston, 2001), which is used as a region of water influx (Appendix A: Figs. A.1, A.2). Both, the J1 and J2 sands contain two reservoirs each, the RA reservoirs to the northeast and the RB reservoirs in the northwest. These reservoirs (RA and RB) are different in hydrocarbon type (Westrich et al., 1999) and separated by a permeability barrier. Pre-production seismic surveys delineate the oil-water contacts in both sands (Swanston, 2001). Gas-oil contacts located in the eastern RA reservoirs are defined by well-logs and production data (Comisky, 2002). Ten years of historical production data, time-lapse seismic results (Swanston, 2001), and a production analysis (Comisky, 2002) indicates that the oil-water contact moves updip with minimal drops in late time pressure. It is assumed that the aquifer size is fixed through time and not increasing, thus the late time pressure support is considered to be due to compaction.

Chapter 2

CHARACTERIZATION AND MODEL OF THE COMPOSITIONAL VARIATION OF THE J1 AND J2 RB RESERVOIRS AT BULLWINKLE

Compositional variation within a single hydrocarbon reservoir is common (Sage et al., 1938; Shulte, 1980; Creek et al., 1985; Hirshberg, 1988; Hoier et al., 2000; Ratulowski et al., 2000). Sage et al. (1938) showed that compositional variation may occur due to thermodynamic equilibrium in a gravitational field. Hirschberg (1988) suggested that compositional variations in oils, with API gravity less than 35° (not close to critical conditions), are caused by asphalt segregation due to gravitational forces. Compositional variations can greatly impact the estimation of fluids in-place (Hirshberg, 1988) as well as the prediction of fluid contacts and saturation changes.

Hoier et al. (2000) described ten possible causes for vertical and horizontal compositional variations and presented a methodology for characterizing and modeling these variations. Further, Hoier et al. (2000) described a methodology for composition interpolation within and extrapolation beyond the PVT data. Creek et al. (1985) presented a case study of a compositionally graded reservoir and described a methodology and theory for predicting phase behavior as a function of depth. Shulte (1980) presented an isothermal gravity-induced equilibrium model for the prediction of compositional variations in depth.

The compositional variation in the J2-RB reservoir is characterized. A 13-component Equation of State (EoS) model is developed and model parameters are constrained based on fluid properties at a reference location in the J2-RB reservoir. At other locations, where PVT data are available, the EoS model predicts the observed phase behavior. The 13-component model is simplified to a 5-component model by lumping the components. The fluid properties of the 5-component model closely duplicate the behavior of the fluids in the PVT data. A linear least-squares regression is used to fit a trend line to the modeled 5-component mole fractions. Finally, two methods of mole fraction extrapolation (constant and linear) are used to predict fluid properties updip where no PVT data are present.

J-sand Fluid Characterization

The J-sands, at Bullwinkle, contain six hydrocarbon reservoirs that are in pressure communication through a common aquifer. The J1-RA, J2-RA, and J3-RB reservoirs are gas-cap reservoirs, the J4-RB is an undersaturated oil reservoir, and the J1-RB and J2-RB are undersaturated, and compositionally graded, reservoirs.

PVT Sample Description

Eight pressure-volume-temperature (PVT) samples were obtained, by Shell Oil Co., from four of the J-sand reservoirs (Table 2-1, Figs. 2-1, 2-2). These PVT samples were collected prior to and during production (Table 2-1). A cross-section of the J-sand RB reservoirs illustrates the fluid types and shows the vertical position of the PVT samples (Figure 2-3). No PVT samples were obtained from the J-sand RA reservoirs.

PVT Sample Properties

The J2-RB reservoir was sampled at 5 locations that span a vertical range of 962.5 feet (Figure 2-3, Table 2-1). With increasing depth, there is a decrease in the proportion

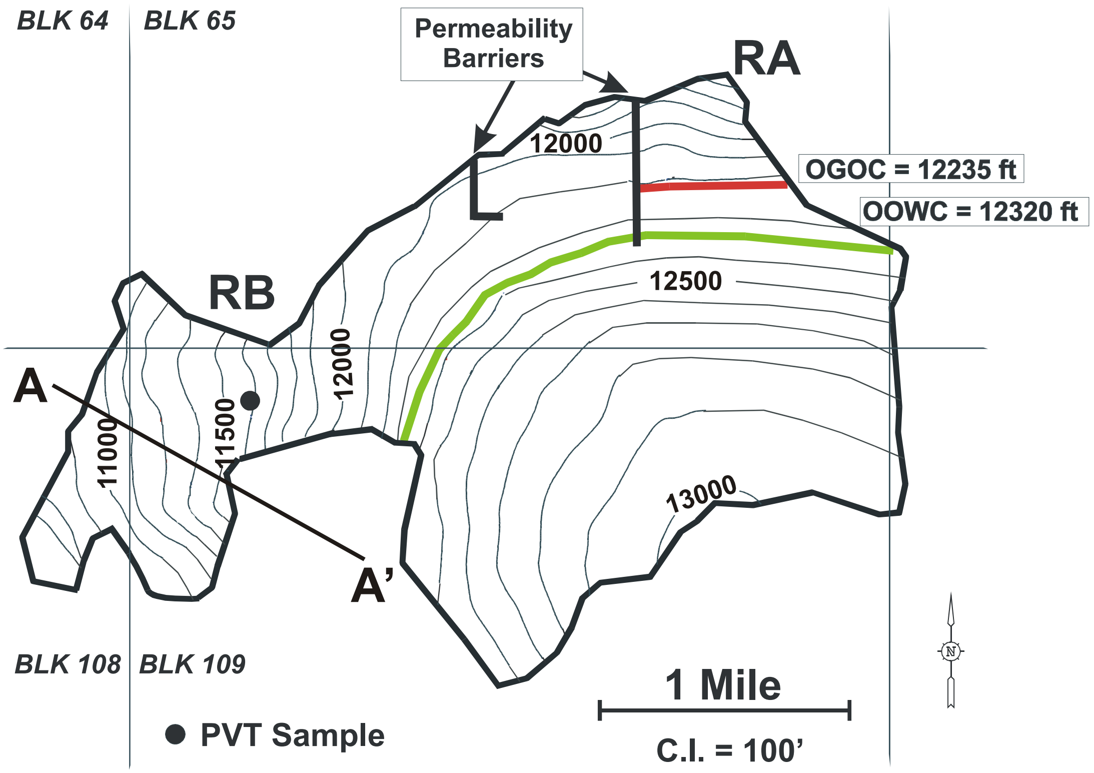
BLK 64
BLK 65
Permeability Barriers
RA
12000
OGOC = 12235 ft
OOWC = 12320 ft
12500
RB
12000
A
11500
11000
13000
A'
BLK 108
BLK 109
1 Mile
N
● PVT Sample
C.I. = 100'

Figure 2-1: J1 sand structure map. Reservoir A (RA) is a gas-cap reservoir separated by a permeability barrier from Reservoir B (RB). One PVT sample (A-1) was obtained from the undersaturated RB reservoir (Table 2-1). Cross-section (A-A') is shown in Figure 2-3. Fluid contacts and sand boundaries are based on seismic and well data (Swanston, 2001).

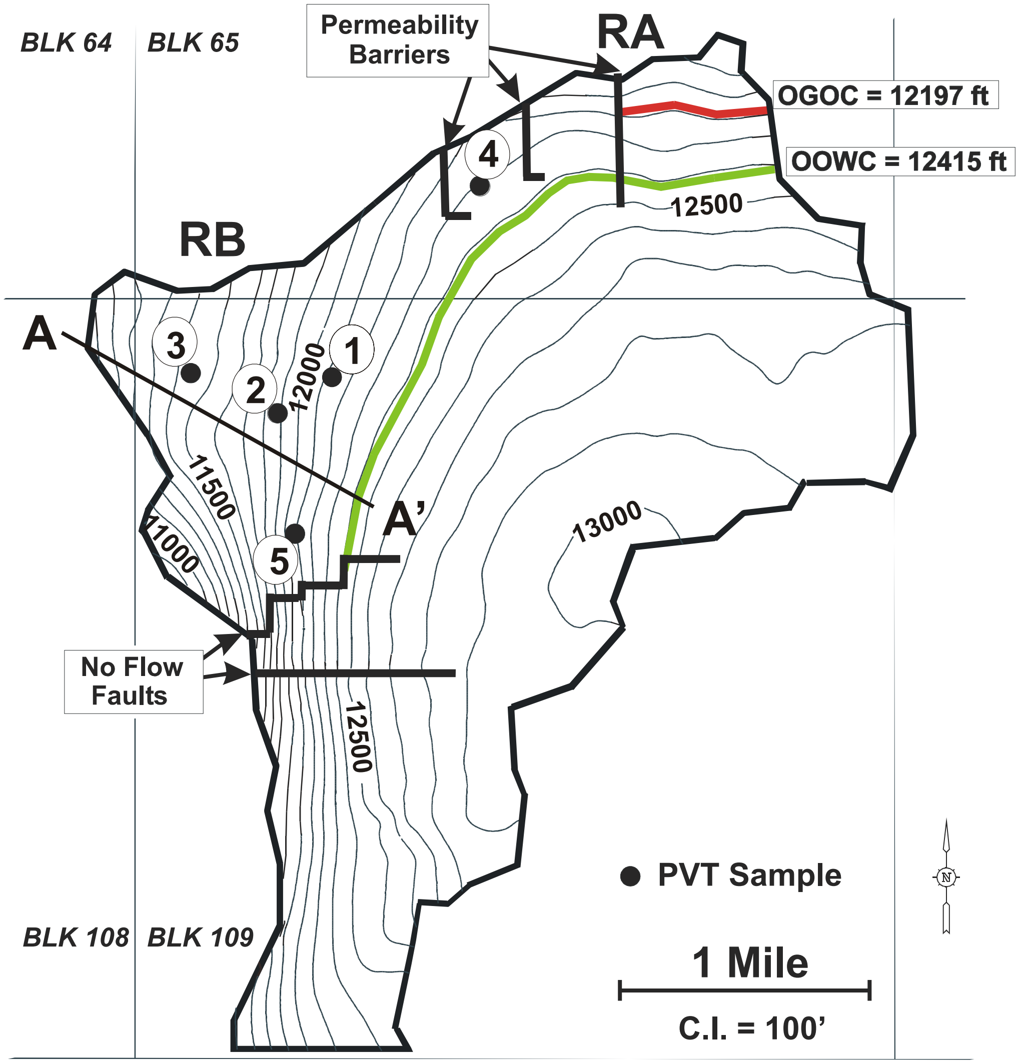
BLK 64
BLK 65
Permeability Barriers
RA
OGOC = 12197 ft
OOWC = 12415 ft
12500
RB
4
A
3
2
12000
1
11500
11000
A'
5
13000
No Flow Faults
12500
PVT Sample
N
BLK 108
BLK 109
1 Mile
C.I. = 100'

Figure 2-2: J2 sand structure map. Reservoir RA is a gas-cap reservoir separated by a permeability barrier from Reservoir RB. Five PVT samples were obtained from the undersaturated RB reservoir: samples 109-1 (#1), A-2-BP (#2), A-3-BP (#3), A-4-BP (#4), and A-5-BP (#5) (Table 2-1). Cross-section (A-A') is shown in Figure 2-3. Fluid contacts and sand boundaries are based on seismic and well data (Swanston, 2001).

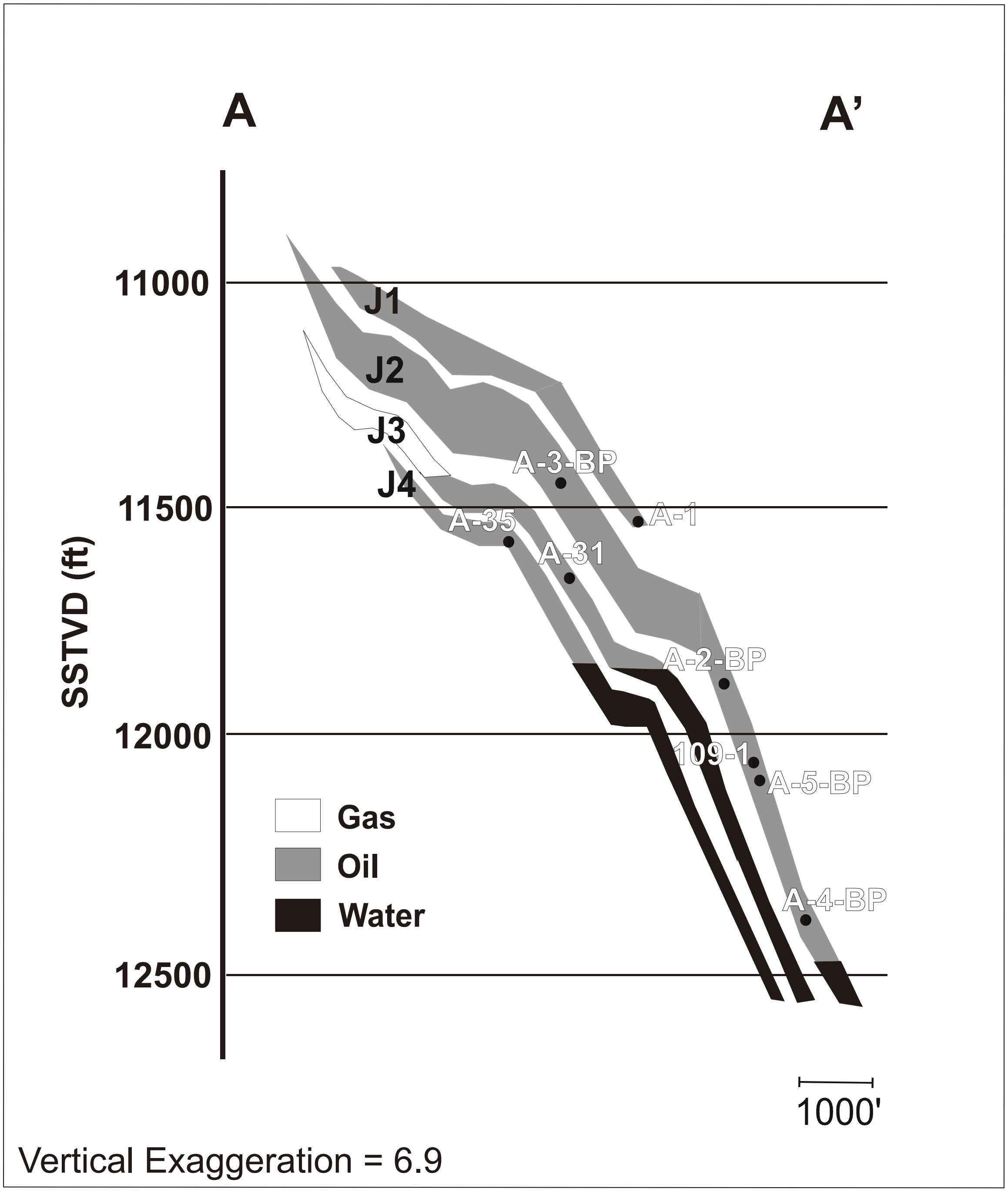
A
A’
11000
11500
12000
12500
SSTVD (ft)
J1
J2
J3
J4
A-3-BP
A-1
A-35
A-31
A-2-BP
109-1
A-5-BP
A-4-BP
Gas
Oil
Water
1000'
Vertical Exaggeration = 6.9

Figure 2-3: Cross-section of J-sand RB reservoirs depicting initial fluid types, fluid contacts, and vertical location of the PVT samples. Map view of the J1 and J2 sands shown in Figs. 2-1 and 2-2, respectively. The J3 and J4 sands are not shown.

Table 2-1: PVT sample data for J-sand reservoirs

Sample #	Well	Reservoir	Sample Date	Initial Reservoir Pressure (psi)	Reservoir Temperature (^oF)	SSTVD (ft)	⌖ Sample Type	* $p_i - p_{sample}$ (psia)
1	A-1	J1-RB	10/24/89	7926	160	11562.2	Surface Sep	95
2	109-1	J2-RB	7/4/84	8487	160	12063.5	RFT	0
3	A-2-BP	J2-RB	10/24/89	8504	163	11886.6	Surface Sep	95
4	A-3-BP	J2-RB	1/30/90	8350	160	11463.4	Surface Sep	160
5	A-4-BP	J2-RB	10/23/89	8653	169	12300.7	Surface Sep	95
6	A-5-BP	J2-RB	1/31/90	8600	162	12099.2	Surface Sep	160
7	A-31	J3-RB	9/23/91	7919	165	11635.3	Surface Sep	560
8	A-35	J4-RB	9/23/91	7881	166	11528.9	Surface Sep	560

* Production while drilling (PWD) operations commenced in July of 1989. The pressure drop from initial pressure (Pi) to the date of the sample pressure (Psample) is recorded in the last column of Table 1. Pi = 8555 psia @ 12070 ft. SSTVD

⌖ Surface Sep refers to fluid samples extracted from the platform test separator and recombined in the laboratory. A Repeat Formation Test tool (RFT) was used to extract fluids from the down whole location in the 109-1 exploration well.

Table 2-2: Reported PVT sample mole fractions for the J1-RB (A-1) and J2-RB

	A-3-BP	A-1	A-2-BP	109-1	A-5BP	A-4-BP
CO_2	0.0016	0.0011	0.0010	0.0006	0.0010	0.0009
N_2	0.0011	0.0011	0.0011	0.0054	0.0025	0.0009
C_1	0.6729	0.6695	0.6398	0.5425	0.6147	0.6038
C_2	0.0413	0.0413	0.0397	0.0389	0.0400	0.0347
C_3	0.0324	0.0333	0.0338	0.0301	0.0353	0.0332
IC_4	0.0072	0.0075	0.0078	0.0070	0.0082	0.0085
NC_4	0.0149	0.0162	0.0164	0.0151	0.0175	0.0175
IC_5	0.0072	0.0076	0.0080	0.0074	0.0088	0.0087
NC_5	0.0090	0.0093	0.0101	0.0091	0.0110	0.0107
C_6	0.0174	0.0222	0.0253	0.0174	0.0243	0.0251
C_{7+}	0.1950	0.1909	0.2170	0.3265	0.2367	0.2560

Table 2-3: Reported PVT sample bubble point pressure fluid properties from differential test for J-sand reservoirs

Well	Depth (ft.)	Reservoir	Bubble Point (psi)	Bo (Res. Bbl/STB)	Differential GOR (SCF/STB)	Viscosity (cp)	Compressibility $(10^{-6}\ psi^{-1})$	Density (gm/cc)
A-3-BP	11463.4	J2-RB	8100	1.772	1752	0.55	11.14	0.6605
A-1	11562.2	J1-RB	7926	1.663	1540	0.57	10.34	0.6886
A-2-BP	11886.6	J2-RB	7038	1.619	1328	0.65	10.97	0.7073
109-1	12063.5	J2-RB	4907	1.382	809	1.03	10.75	0.7395
A-5-BP	12099.2	J2-RB	6125	1.513	1118	0.77	10.53	0.7074
A-4-BP	12300.7	J2-RB	5800	1.450	971	0.88	10.52	0.7151
A-31	11494.0	J3-RB	7919	1.462	1085	1.26	8.87	0.7285
A-35	11309.9	J4-RB	7881	1.487	1183	1.20	8.89	0.7262

of Methane (C_1) and an increase in the proportion of the heavier hydrocarbons (C_{7+}) (Figure 2-4). Changes with depth in the mid-range hydrocarbons, CO_2, and N_2 are small relative to these changes (Figure 2-5, Table 2-2). The methane and C_{7+} components make up 86% of the molecules of the hydrocarbon mixture, making them the controlling hydrocarbon components of the fluid properties (Figure 2-5, Table 2-2).

The fluid properties reflect the change in composition that is observed (Table 2-3). The bubble point pressure (p_{sat}) and the differential gas-oil ratio (GOR) decrease with depth (Figs. 2-6, 2-7). The density and viscosity increase with depth (Figs. 2-8, 2-9). The formation volume factor (*Bo*) and the oil compressibility decrease with depth (Figs. 2-10, 2-11). The 109-1 sample does not fall within the trend defined by the other samples; contamination by drilling fluids was reported, and we interpret that these data do not reflect the in-situ fluid properties.

These data indicate that the J1 and J2 RB reservoirs are compositionally graded. Hirschberg (1988) stated that light hydrocarbon fluids (30^{o} API), with high asphaltene concentrations (greater than 5%), will result in strong compositional variations. The J1-RB and J2-RB have asphaltene concentrations of 9.1% and 11%, respectively (Table 2-4), thus the observed compositional variation at Bullwinkle is comparable with Hirschberg's prediction.

The J1-RB sample has fluid properties and compositions that lie within the trends defined by the J2-RB (Figs. 2-4 through 2-11). We interpret that it records the same compositional grading that is present in the J2-RB.

The J3-RB and J4-RB reservoirs are different (Figs. 2-6 through 2-11). The PVT fluid properties (p_{sat}, GOR, density, viscosity, and *Bo*) do not lie along the same trend as

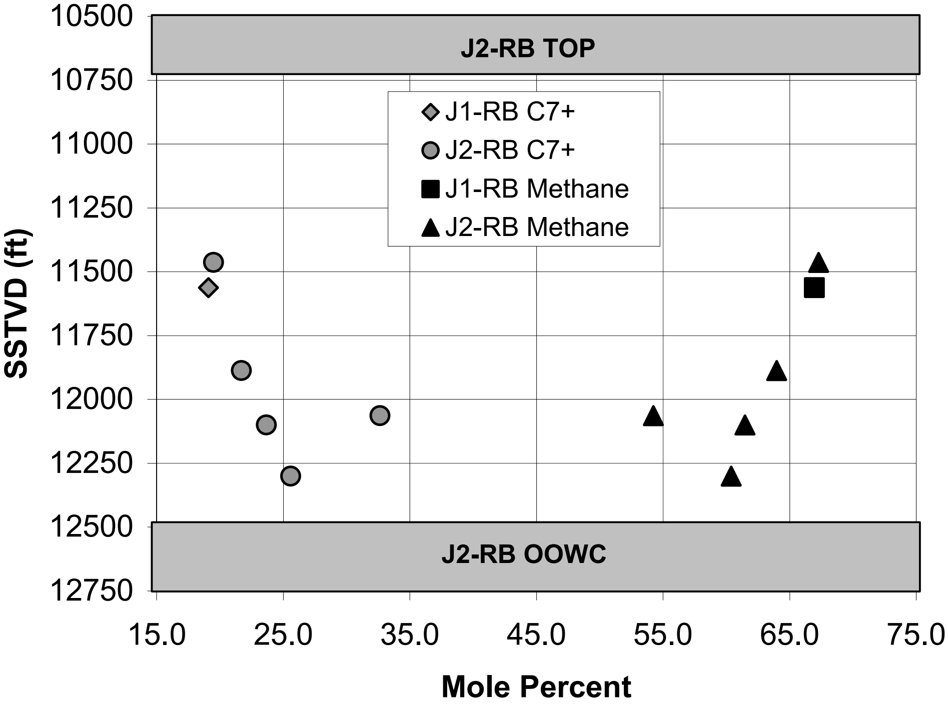

Figure 2-4: Depth versus methane and C_{7+} mole percent for the J1-RB (A-1) and J2-RB PVT samples (Table 2-2). The values, from top to bottom, are for the A-3-BP, A-1, A-2-BP, 109-1, A-5-BP, and A-4-BP sample locactions. The 109-1 PVT sample was collected using a bottom hole RFT that report contaminants.

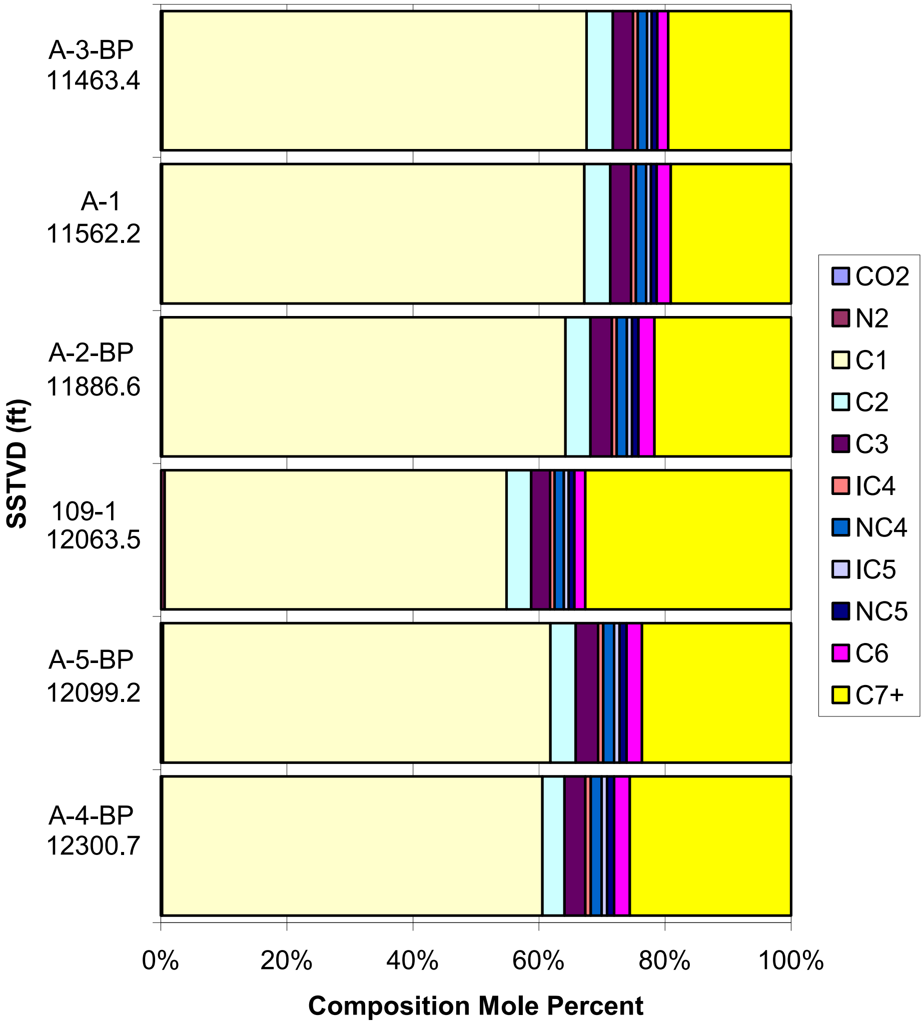

Figure 2-5: J1-RB (A-1) and J2-RB PVT sample compositions (Table 2-2). The 109-1 PVT sample was collected using a bottom hole RFT that report contaminants.

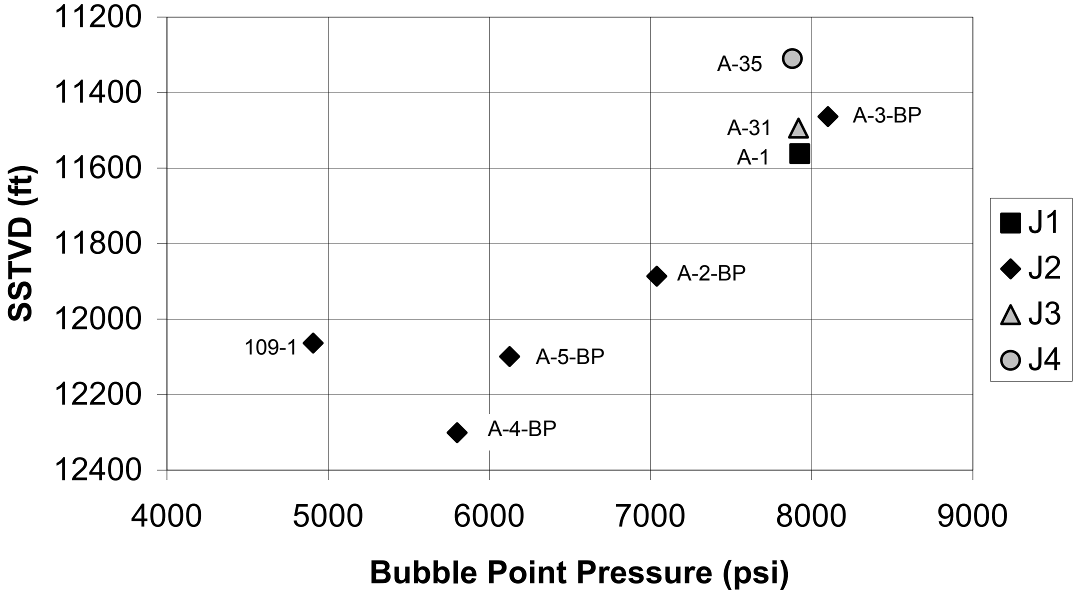

Figure 2-6: Depth versus bubble point pressure for J-RB PVT samples (Table 2-3). The J1-RB and J2-RB reservoirs show a near linear trend in depth except for the 109-1 sample. The 109-1 sample was collected using a bottom hole RFT that report contaminants. All other samples were collected from the platform test separator.

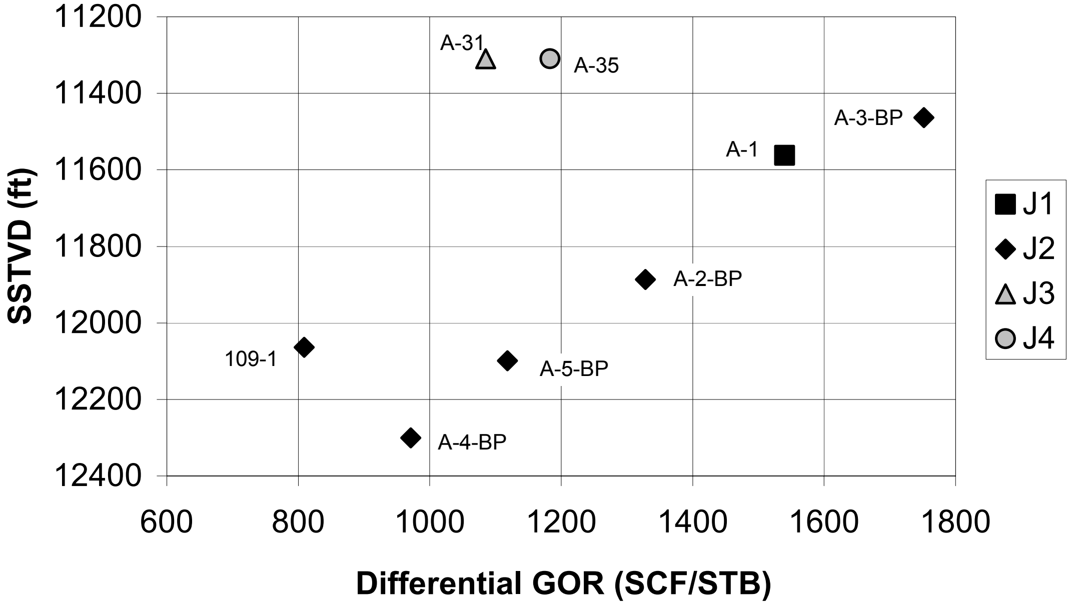

Figure 2-7: Depth versus differential test gas-oil ratio at bubble point pressure for J-RB PVT samples (Table 2-3). A near linear trend of GOR in depth is observed for the J1-RB and J2-RB reservoirs.

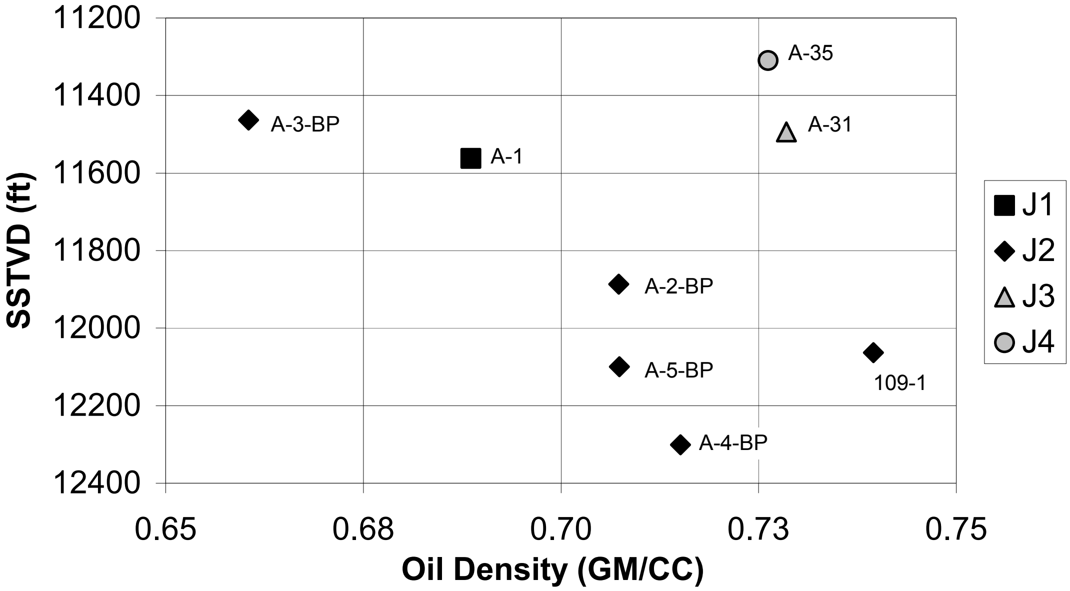

Figure 2-8: Depth versus oil density (ρ) at bubble point pressure for J-RB PVT samples (Table 2-3). A near linear trend of density in depth is observed for the J1-RB and J2-RB reservoirs.

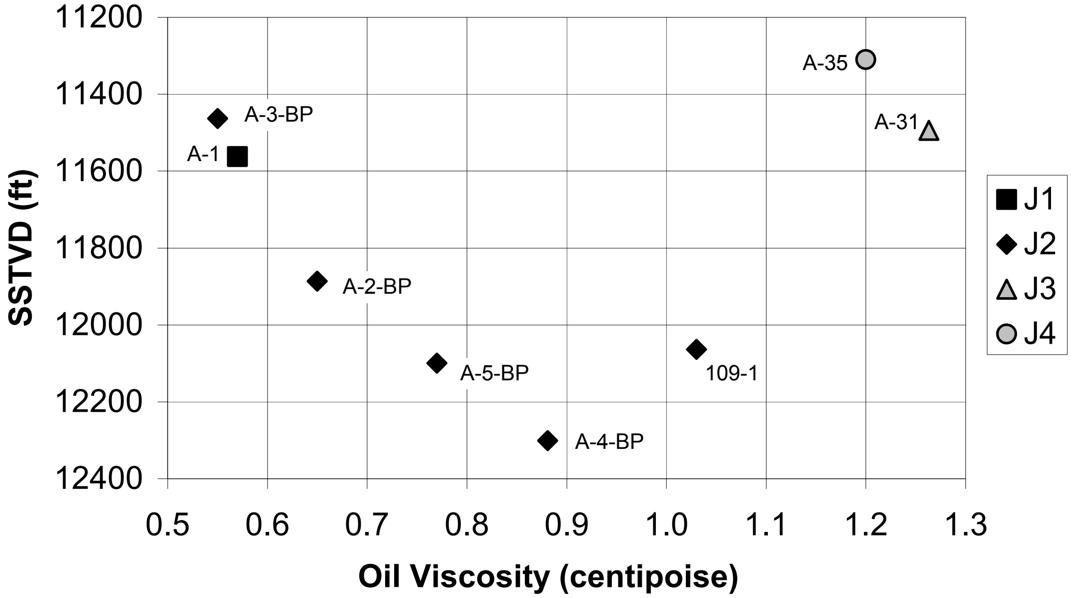

Figure 2-9: Depth versus oil viscosity (μ) at bubble point pressure for J-RB PVT samples (Table 2-3). A near linear trend of oil viscosity in depth is observed for the J1-RB and J2-RB reservoirs.

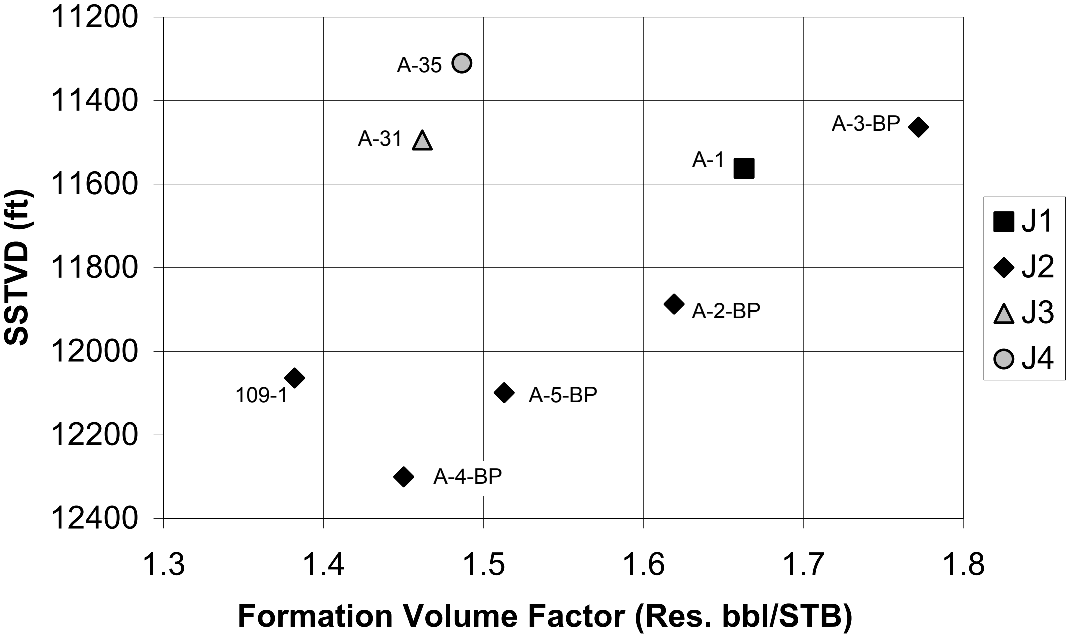

Figure 2-10: Depth versus formation volume factor (*Bo*) at bubble point pressure for J-RB PVT samples (Table 2-3). A near linear trend of Bo in depth is observed for the undersaturated J2-RB and J1-RB reservoirs.

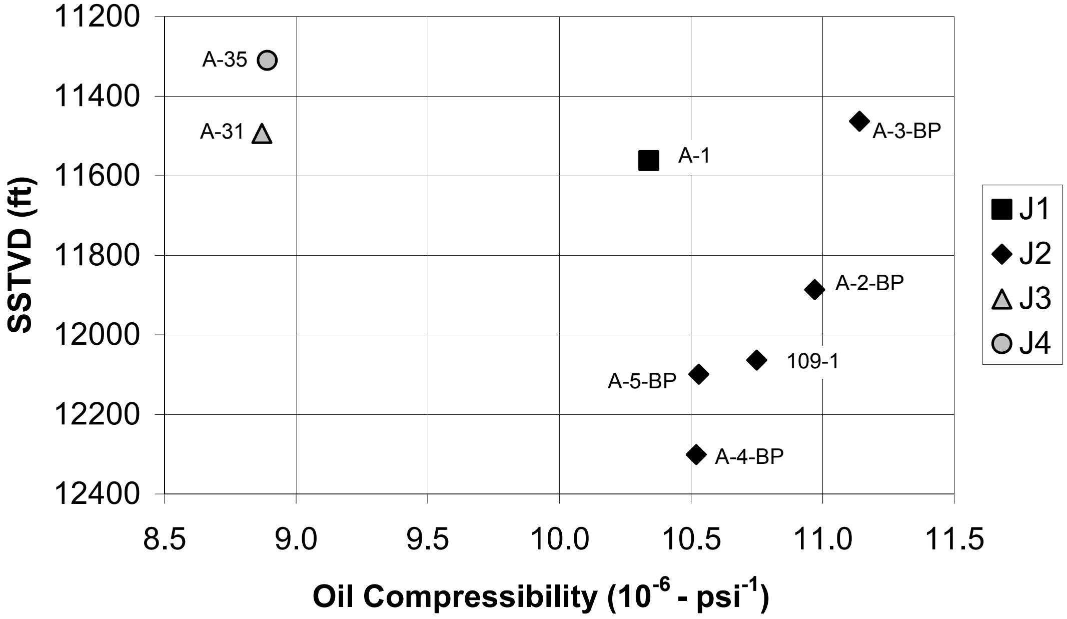

Figure 2-11: Depth versus oil compressibility (*c*) at bubble point pressure for J-RB PVT samples (Table 2-3). A near linear trend of oil compressibility in depth is observed for the J2-RB reservoir.

Table 2-4: Reported PVT sample C_{7+} properties for the J1-RB and J2-RB

Well	Depth (ft.)	Reservoir	Mole Fraction	MW (gm/mole)	Specific Gravity	Weight % of Asphaltenes
A-3-BP	11463.4	J2-RB	0.1950	268.9	0.8898	-
A-1	11562.2	J1-RB	0.1909	282.2	0.8915	9.1
A-2-BP	11886.6	J2-RB	0.2170	289.7	0.8992	11.0
A-5-BP	12099.2	J2-RB	0.2367	273.7	0.8936	-
A-4-BP	12300.7	J2-RB	0.2560	297.5	0.9022	-

Table 2-5: PVT sample multi-stage separator GOR, producing GOR, and recombination GOR

Well	Reservoir	SSTVD (ft)	PVT Multi-Stage Separator GOR (SCF/STB)	Producing GOR (SCF/STB)	PVT Sample Recombination GOR (SCF/STB)
A-3-BP	J2-RB	11463.2	1541	1420	1039
A-1	J1-RB	11511.2	1469	1460	1023
A-2-BP	J2-RB	11886.6	1234	1160	812
A-5-BP	J2-RB	12099.2	1096	925	685
A-4-BP	J2-RB	12300.7	840	830	593

that of the J2-RB. Further, the J3-RB fluid is reported to be saturated at initial conditions (Figure 2-3). The different fluid properties indicate separate hydrocarbon accumulations.

Initial Production Behavior

The initial production data, pressure and gas-oil ratio, are evaluated to gain insight into reservoir connectivity and the PVT data. The J1, J2, J3, and J4 sands are in pressure communication (Appendix A), implying that these reservoirs are interconnected. The J2-RB producing GOR, decreases with depth (Figure 2-12). This is compatible with the compositional trend that is present in the PVT data.

Both the producing GOR and the PVT multistage separator GOR decrease with depth and the producing GOR is consistently lower than the PVT multi-stage separator GOR (Figure 2-13, Table 2-5). PVT samples were collected from a surface separator and recombined to a measured GOR (Table 2-5). The inaccuracies associated with this GOR measurement (Wang et al., 2001) may account for GOR differences.

The J3-RB and J4-RB reservoirs show a different producing trend than the J1-RB and J2-RB reservoirs. PVT data indicate that the J3-RB and J4-RB reservoirs were originally a gas-cap reservoir and an undersaturated oil reservoir, which is confirmed by the production data.

Conclusions

The J2-RB reservoir is an undersaturated, compositionally graded, oil reservoir. Five PVT samples show a near-linear gradation in composition and fluid properties in depth. Only one PVT sample is available in the J1-RB reservoir. However, the composition and fluid properties lie along the trend defined by the J2-RB. Based on this,

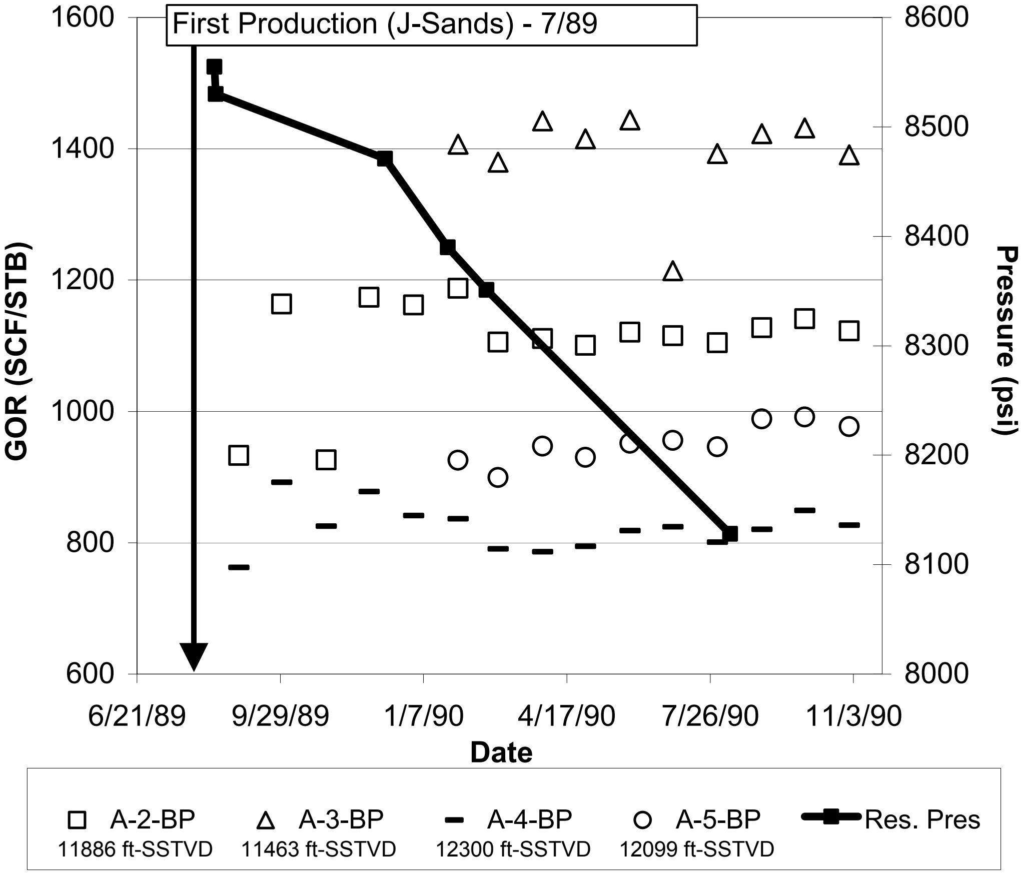

Figure 2-12: Initial producing GOR and reservoir pressure versus time for J2-RB wells (Table 2-5). Initial producing GOR varies by 600 SCF/STB over an 800 ft. interval. The arrow represents the initial production date in the J-sands. Pressure data shown are from Shell Offshore Inc. and are referenced to a 12070 ft., SSTVD, datum (Appendix A).

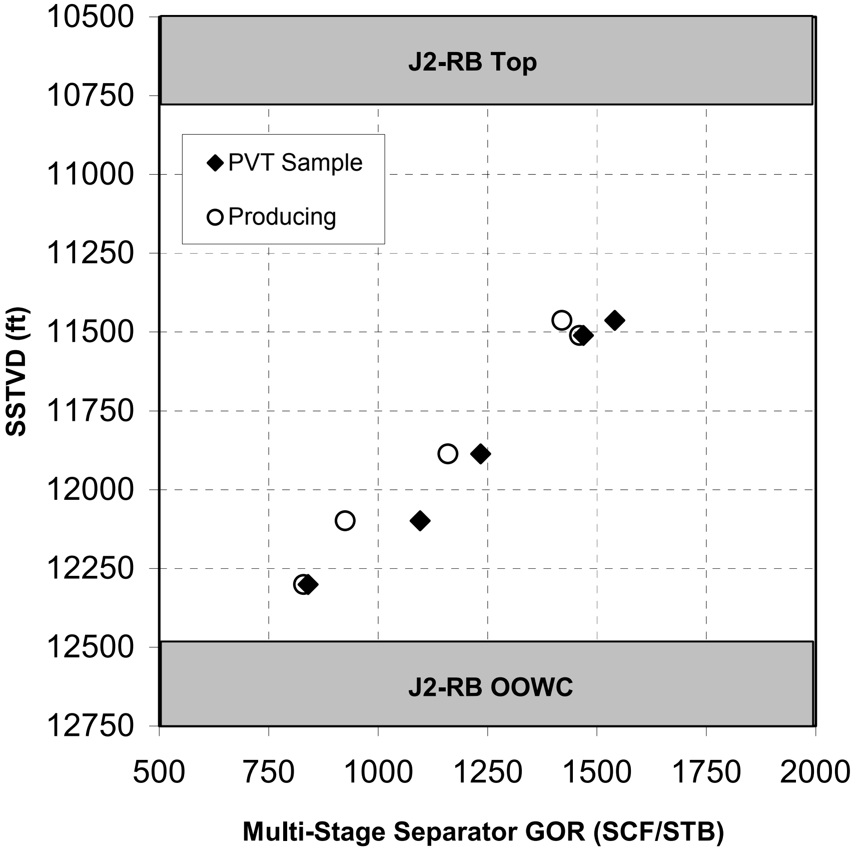

Figure 2-13: Comparison of the initial producing GOR and PVT sample multi-stage separator GOR, for J1-RB and J2-RB samples (Table 2-5). Data suggests that the recombined PVT samples are not representative of the in-situ fluids. PVT samples were recombined to a measured GOR measured from a 4-hour test. GOR values shown, from top to bottom, are from the A-3-BP (J2-RB), A-1 (J1-RB), A-2-BP (J2-RB), A-5-BP (J2-RB), and A-4-BP (J2-RB) sample locations.

the J1-RB reservoir is interpreted to be compositionally graded with similar fluids to that of the J2-RB. Additionally, the PVT sample compositions are observed to be lighter than the in-situ fluids.

The J3-RB and J4-RB reservoirs contain different fluid types than the J1-RB and J2-RB reservoirs but are in pressure communication. PVT and production differences observed in the J3-RB and J4-RB reservoirs suggest that communication must be present beneath the oil-water contact for these reservoirs.

Model Development

A compositional fluid model has been constructed for the J1 and J2 sands to model fluid properties. A flow chart outlining the modeling procedure used here is presented in Figure 2-14. The compositional model is developed using the Peng-Robinson (PR) Equation of State (EoS) (Peng and Robinson, 1976). The model is based on a PVT sample from which C_{7+} pseudo-components are derived, combined with pure components, and tuned to match PVT data. The EoS model is lumped into a 5-component model to reduce model complexity. The mole fractions of the PVT samples are adjusted to match producing GOR. Finally, the adjusted mole fractions are fit with a linear least squares regression, using linear and constant extrapolations updip beyond the last known PVT data.

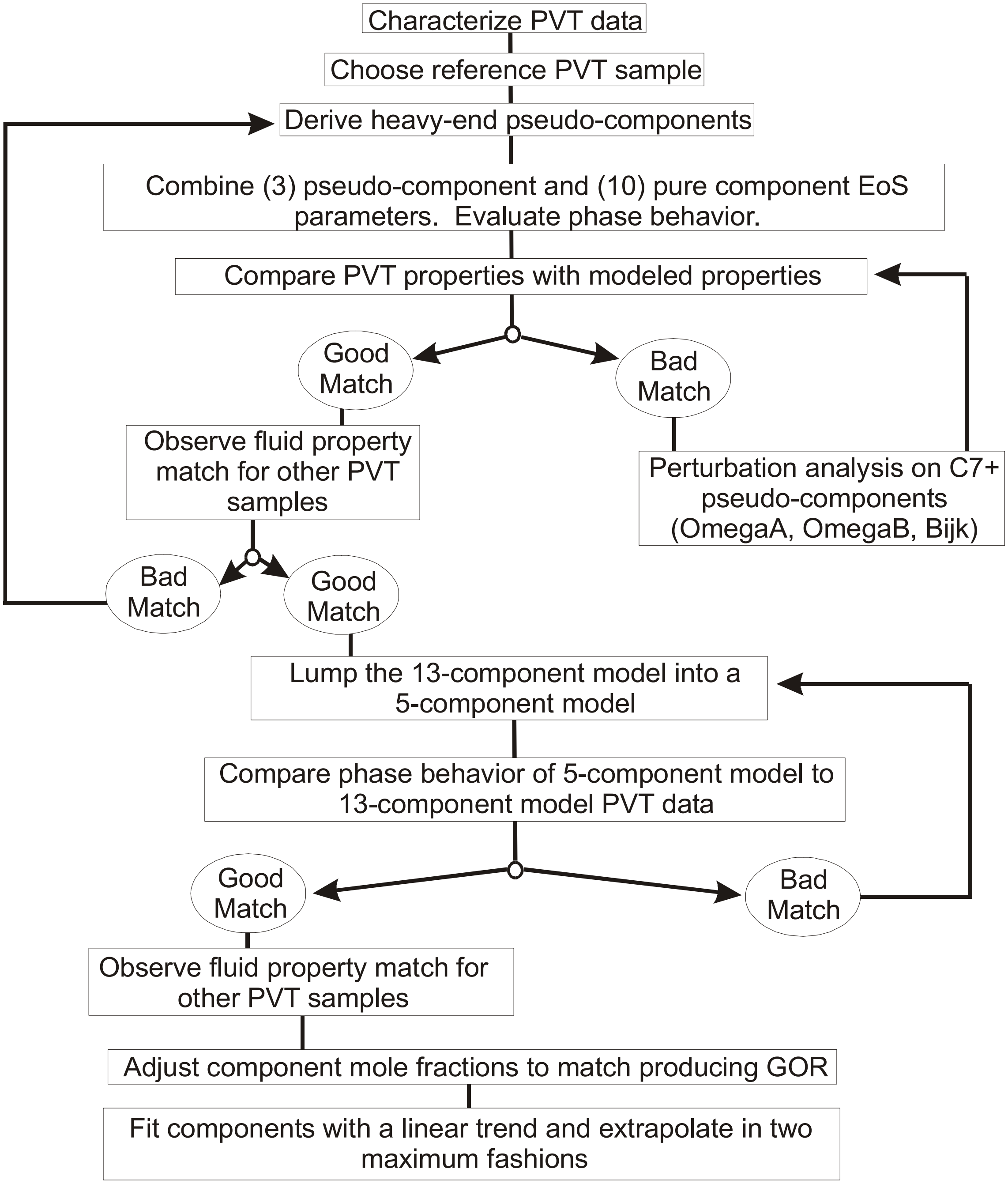
Characterize PVT data
Choose reference PVT sample
Derive heavy-end pseudo-components
Combine (3) pseudo-component and (10) pure component EoS parameters. Evaluate phase behavior.
Compare PVT properties with modeled properties
Good Match
Bad Match
Observe fluid property match for other PVT samples
Perturbation analysis on C7+ pseudo-components (OmegaA, OmegaB, Bijk)
Bad Match
Good Match
Lump the 13-component model into a 5-component model
Compare phase behavior of 5-component model to 13-component model PVT data
Good Match
Bad Match
Observe fluid property match for other PVT samples
Adjust component mole fractions to match producing GOR
Fit components with a linear trend and extrapolate in two maximum fashions

Figure 2-14: Procedure for fluid property modeling.

Reference PVT Sample

Padua (1997) suggested that, for a compositionally graded reservoir, an EoS model should be developed using a sample at a middip location within the hydrocarbon column. The A-2-BP PVT sample was chosen as the reference sample in the J2-RB reservoir (Figs. 2-2, 2-3).

The PVT properties, from the reference sample, are used to develop a single set of EoS parameters that describe the volumetric and phase behavior of the J1 and J2 fluids. The heavy end (C_{7+}) EoS parameters that are derived are tuned to match PVT data from constant mass expansion, differential liberation, flash liberation, and multi-stage separator experiments (Tables 2-6, through 2-10).

Derivation of Heavy End Pseudo-Components

DESKTOP-PVT version 1998.1 was used to model the behavior of the C_{7+} heavy ends. The heavy end properties, from the reference sample, were modeled using Coat's (1985) approach (Table 2-11). Three pseudo-components (H1, H2, and H3) were derived based on PVT reported C_{7+} specific gravity, molecular weight, and mole fraction (Tables 2-12, 2-13). The C_{7+} heavy ends were treated as a continuous distribution that is divided into three groups based on molecular weight (M.W.) ranges. The set of molecular weight ranges used here were; H1 = 96 to 250, H2 = 250 to 300, and H3 = 300 to 539.

The C_{7+} EoS parameter correlations for critical temperature (T_c), critical pressure (P_c), and acentric factor (w) are based on work performed by Pederson et al. (1984). The Cavett correlation (Cavett, 1962) was used to determine T_c and P_c for each pseudo-component. The Riazi-Daubert correlation (Riazi and Daubert, 1980) was used to determine the critical compressibility (z_c) for each pseudo-component. The Kesler-Lee

Table 2-6: Constant mass expansion PVT data for the A-2-BP

Pressure (psia)		Bt (V/Vsat)	Density (gm/cc	Compressibility (10^{-6} psi^{-1})	‘Y' Function
9000		0.9801	0.7217	9.49	-
8504	Res.	0.9849	0.7181	9.65	-
8000		0.9898	0.7146	9.92	-
7500		0.9950	0.7109	10.34	-
7038	B.P.	1.0000	0.7073	10.97	-
(TWO PHASE)					
6300		1.0155	0.6965	-	7.539
5600		1.0363	0.6825	-	7.065
4900		1.0662	0.6634	-	6.59
4200		1.1105	0.6369	-	6.116
3500		1.1792	0.5998	-	5.642
2800		1.2929	0.5471	-	5.167
2100		1.5011	0.4712	-	4.693
1400		1.9546	0.3619	-	4.219
700		3.4182	0.2069	-	3.744

Table 2-7: Differential liberation PVT data for the A-2-BP. The (*) represents the Bo and GOR for multi-stage separator conditions

Pressure (psia)		Oil Density (gm/cc)	Bo (Res. Bbl/STB)	Bo* (Res. Bbl/STB)	Oil Compressibility (10^{-6} psi^{-1})	Differential GOR (SCF/STB)	Multi-Stage Separator GOR (SCF/STB)	Oil Viscosity (cp)
9000		0.7217	1.5871	1.4671	9.49	1328	1234	0.920
8504	Res.	0.7181	1.5948	1.4743	9.65	1328	1234	0.852
8000		0.7146	1.6028	1.4816	9.92	1328	1234	0.782
7500		0.7109	1.6112	1.4894	10.34	1328	1234	0.714
7038	B.P.	0.7073	1.6193	1.4969	10.97	1328	1234	0.650
6300		0.7243	1.5335	1.4176	8.52	1140	1039	0.748
5600		0.739	1.4639	1.3532	7.98	982	914	0.819
4900		0.7512	1.4071	1.3007	7.53	845	787	0.934
4200		0.7622	1.3577	1.2551	7.13	721	672	1.067
3500		0.7736	1.3108	1.2117	6.78	603	564	1.209
2800		0.7854	1.2655	1.1698	6.43	489	458	1.407
2100		0.7976	1.2218	1.1294	6.11	378	355	1.650
1400		0.8107	1.1778	1.0887	5.79	266	251	2.176
700		0.8262	1.1326	-	5.5	160	-	3.296
15		0.8504	1.0470	-	-	-	-	6.749
15	@60F	0.8904	1.0000	-	-	-	-	-

Table 2-8: Gas differential liberation PVT data for the A-2-BP

Pressure (psia)	Specific Gravity (Air = 1.00)		Deviation Factor (z)	Barrels of Gas in Reservoir per MMCF (Bg)	Bt	Calculated Viscosity (cp)
	Increm.	Accum.				
7038	(Saturation Pressure)					
6300	0.8290	0.829	1.168	594	1.6450	0.0394
5600	0.8192	0.8245	1.062	608	1.6744	0.0374
4900	0.8102	0.8204	0.975	638	1.7155	0.0343
4200	0.8022	0.8167	0.916	699	1.7825	0.030
3500	0.7957	0.8133	0.883	809	1.8974	0.025
2800	0.7902	0.8102	0.865	990	2.0970	0.021
2100	0.787	0.8075	0.868	1325	2.4814	0.0174
1400	0.7875	0.8054	0.895	2050	3.3557	0.0147
700	0.8112	0.8059	0.941	4310	6.1684	0.0128
15.025	1.2762	0.8624	1.000	213392	284.4421	0.0102

Table 2-9: Flash liberation PVT data for the A-2-BP

Type of Liberation	GOR (SCF/STB)	Bo (Res. Bbl/STB)	Stock Tank Gravity API @ 60°F	Gas Gravity Air = 1.00
Reservoir oil to 0.0 psig & 70 °F	1234	1.4969	29.6	0.6595
Res. oil flash to 0.0 psig & 70 °F	1297	1.6025	27.6	0.8476
Differential @ 160 °F	1328	1.6193	27.3	0.8624

Table 2-10: Multi-stage separator PVT data for the A-2-BP

Separator Pressure (psi)	Separator Temperature (°F)	Multi-Stage Separator GOR (SCF/STB)	Gas Gravity Air = 1.00
1500	165	916	0.6268
500	85	168	0.6422
70	85	97	0.7783
35	60	30	0.8877
15.025	60	23	1.2904

Table 2-11: C_{7+} properties from the A-2-BP

Molecular weight	289.70
Specific gravity	0.8992
Mole fraction	0.2170

Table 2-12: Derived heavy-end pseudo-component parameters for the A-2-BP

Name	M.W.	T_c (^oF)	P_c (psi)	Z_c	w	Omega A	Omega B	Parachor	Mole Fraction
H1	159.85	709.6	333.8	0.2710	0.5021	0.4572356	0.077796	507.98	0.11843
H2	271.01	990.6	192.8	0.2119	0.7623	0.4572356	0.077796	820.30	0.02125
H3	493.72	1359.	183.8	0.2899	1.2217	0.4572356	0.077796	1635.00	0.07732

Table 2-13: Derived heavy-end C_1 binary interaction parameters

Name	C_1 Binary Interaction Parameter
H1	0.04394
H2	0.05428
H3	0.06913

correlation (Kesler and Lee, 1976) was used to determine *w* for each pseudo-component. Whitson (1984) gives a detailed discussion of these correlations.

The methane-C_{7+} binary interaction parameters are calculated based on a correlation presented by Nghiem et al. (1986). These parameters are based on pure components and therefore are tuned, along with *Omega A* and *Omega B*, to match PVT fluid properties.

Tuning the Parameters of the 13-Component Model

The cubic EoS cannot accurately predict the phase behavior of a hydrocarbon system without EoS parameter adjustment, otherwise known as "tuning" (Nitcha, 2001; Coats, 1985). Tuning is required due to the semi-empirical basis of the EoS parameters for the derived C_{7+} pseudo-components (Nitcha, 2001).

The three pseudo-components and their EoS parameters are combined with ten PVT reported pure components (CO_2, N_2, C_1, C_2, C_3, IC_4, NC_4, IC_5, NC_5, C_6) (Tables 2-14, 2-15). Pure component EoS parameters are from an internal database located in DESKTOP-PVT (DESKTOP-PVT Manual, 1996) and are also found in other texts (Ahmed, 1989).

The 13-component EoS model is tuned to match the PVT properties of the reference well. PVT property matches are accomplished through a perturbation analysis (Coats, 1985) on the C_{7+} pseudo-component parameters (*Omega A*, *Omega B*, and methane binary interaction parameters) (Tables 2-16, 2-17). This perturbation minimizes the sum of the squared deviations between calculated and experimental PVT values. The simulated property matches, for the reference well (A-2-BP), result in less than 6% deviation from the PVT data (Tables 2-19, 2-20).

Table 2-14: 13-Component Peng-Robinson EoS model for the A-2-BP

	M.W.	T_c (^oF)	P_c (psi)	Z_c	w	Omega A	Omega B	Parachor	Mole Fraction
CO_2	44.01	87.9	1070.9	0.2742	0.2225	0.4572356	0.077796	49.6	0.0010
N_2	28.013	-232.4	493.0	0.2910	0.0372	0.4572356	0.077796	35.0	0.0011
C_1	16.043	-116.6	667.8	0.2703	0.0126	0.4572356	0.077796	71.0	0.6398
C_2	30.07	90.1	707.8	0.2850	0.0978	0.4572356	0.077796	111.0	0.0397
C_3	44.097	206.0	616.3	0.2810	0.1541	0.4572356	0.077796	151.0	0.0338
IC_4	58.124	275.0	529.1	0.2830	0.1840	0.4572356	0.077796	191.0	0.0078
NC_4	58.124	305.7	550.7	0.2740	0.2015	0.4572356	0.077796	191.0	0.0164
IC_5	72.151	369.1	490.4	0.2730	0.2286	0.4572356	0.077796	231.0	0.0080
NC_5	72.151	385.7	488.6	0.2620	0.2524	0.4572356	0.077796	231.0	0.0101
C_6	86.178	453.7	436.9	0.3878	0.2998	0.4572356	0.077796	271.0	0.0253
H1	159.85	709.6	333.8	0.2710	0.5021	0.4572356	0.077796	508.0	0.1184
H2	271.01	990.6	192.8	0.2119	0.7623	0.4572356	0.077796	820.3	0.0213
H3	493.72	1359.0	183.8	0.2899	1.2217	0.4572356	0.077796	1635.0	0.0773

Table 2-15: Binary interaction parameters for the 13-component model

	CO_2	N_2	C_1	C_2	C_3	IC_4	NC_4	IC_5	NC_5	C_6	H1	H2
N_2	0.0											
C_1	0.15	0.0										
C_2	0.15	0.12	0.0									
C_3	0.15	0.12	0.0	0.0								
IC_4	0.15	0.12	0.02	0.01	0.01							
NC_4	0.15	0.12	0.02	0.01	0.01	0.0						
IC_5	0.15	0.12	0.02	0.01	0.01	0.0	0.0					
NC_5	0.15	0.12	0.02	0.01	0.01	0.0	0.0	0.0				
C_6	0.15	0.12	0.025	0.01	0.01	0.0	0.0	0.0	0.0			
H1	0.15	0.12	0.04394	0.01	0.01	0.0	0.0	0.0	0.0	0.0		
H2	0.15	0.12	0.05428	0.01	0.01	0.0	0.0	0.0	0.0	0.0	0.0	
H3	0.15	0.12	0.06913	0.01	0.01	0.0	0.0	0.0	0.0	0.0	0.0	0.0

Table 2-16: Tuned 13-component EoS model for the A-2-BP. Tuned values are in bold.

	M.W.	T_c (°F)	P_c (psi)	Z_c	w	Omega A	Omega B	Parachor	Mole Fraction
CO_2	44.01	87.9	1070.9	0.2742	0.2225	0.4572356	0.077796	49.60	0.0010
N_2	28.013	-232.4	493.0	0.2910	0.0372	0.4572356	0.077796	35.00	0.0011
C_1	16.043	-116.6	667.8	0.2703	0.0126	0.4572356	0.077796	71.00	0.6398
C_2	30.07	90.1	707.8	0.2850	0.0978	0.4572356	0.077796	111.00	0.0397
C_3	44.097	206.0	616.3	0.2810	0.1541	0.4572356	0.077796	151.00	0.0338
IC_4	58.124	275.0	529.1	0.2830	0.1840	0.4572356	0.077796	191.00	0.0078
NC_4	58.124	305.7	550.7	0.2740	0.2015	0.4572356	0.077796	191.00	0.0164
IC_5	72.151	369.1	490.4	0.2730	0.2286	0.4572356	0.077796	231.00	0.0080
NC_5	72.151	385.7	488.6	0.2620	0.2524	0.4572356	0.077796	231.00	0.0101
C_6	86.178	453.7	436.9	0.3878	0.2998	0.4572356	0.077796	271.00	0.0253
H1	159.85	709.6	333.8	0.2710	0.5021	**0.3512520**	**0.054459**	508.0	0.1184
H2	271.01	990.6	192.8	0.2119	0.7623	**0.3200690**	**0.072783**	820.3	0.0213
H3	493.72	1359.0	183.8	0.2899	1.2217	**0.320202**	**0.079184**	1635.0	0.0773

Table 2-17: Tuned binary interaction parameters for the 13-component model. Tuned values are in bold.

	CO_2	N_2	C_1	C_2	C_3	IC_4	NC_4	IC_5	NC_5	C_6	H1	H2
N_2	0.0											
C_1	0.15	0.0										
C_2	0.15	0.12	0.02									
C_3	0.15	0.12	0.02	0.0								
IC_4	0.15	0.12	0.02	0.01	0.01							
NC_4	0.15	0.12	0.02	0.01	0.01	0.0						
IC_5	0.15	0.12	0.02	0.01	0.01	0.0	0.0					
NC_5	0.15	0.12	0.02	0.01	0.01	0.0	0.0	0.0				
C_6	0.15	0.12	0.025	0.01	0.01	0.0	0.0	0.0	0.0			
H1	0.15	0.12	**0.19073**	0.01	0.01	0.0	0.0	0.0	0.0	0.0		
H2	0.15	0.12	**0.07092**	0.01	0.01	0.0	0.0	0.0	0.0	0.0	0.0	
H3	0.15	0.12	**0.02021**	0.01	0.01	0.0	0.0	0.0	0.0	0.0	0.0	0.0

Table 2-18: 13-component model compositions from PVT data and derived pseudo-component compositions

Name	A-3-BP	A-1	A-2-BP	A-5BP	A-4-BP
CO_2	0.0016	0.0011	0.0010	0.0010	0.0009
N_2	0.0011	0.0011	0.0011	0.0025	0.0009
C_1	0.6729	0.6695	0.6398	0.6147	0.6038
C_2	0.0413	0.0413	0.0397	0.0400	0.0347
C_3	0.0324	0.0333	0.0338	0.0353	0.0332
IC_4	0.0072	0.0075	0.0078	0.0082	0.0085
NC_4	0.0149	0.0162	0.0164	0.0175	0.0175
IC_5	0.0072	0.0076	0.0080	0.0088	0.0087
NC_5	0.0090	0.0093	0.0101	0.0110	0.0107
C_6	0.0174	0.0222	0.0253	0.0243	0.0251
H1	0.1155	0.1140	0.1184	0.1222	0.1260
H2	0.0190	0.0139	0.0213	0.0235	0.0250
H3	0.0605	0.0630	0.0773	0.0910	0.1050

Table 2-19: Reported PVT sample properties at reservoir conditions

Well	Depth (ft.)	Reservoir	Bubble Point (psi)	Bo (Res. Bbl/STB)	Differential GOR (SCF/STB)	Viscosity (cp)	Density (gm/cc)	Multi-Stage Separator GOR (SCF/STB)
A-3-BP	11463.4	J2-RB	8100	1.7670	1752	0.561	0.6624	1541
A-1	11562.2	J1-RB	7926	1.6553	1540	0.577	0.6918	1469
A-2-BP	11886.6	J2-RB	7038	1.5948	1328	0.852	0.7181	1234
A-5-BP	12099.2	J2-RB	6125	1.4770	1118	0.899	0.7246	1096
A-4-BP	12300.7	J2-RB	5800	1.4151	971	1.214	0.7329	840

Table 2-20: Tuned 13-component model fluid properties at reservoir conditions

Well	Depth (ft.)	Reservoir	Bubble Point (psi)	Bo (Res. Bbl/STB)	Differential GOR (SCF/STB)	Viscosity (cp)	Density (gm/cc)	Multi-Stage Separator GOR (SCF/STB)
A-3-BP	11463.4	J2-RB	8143	1.7002	1717	0.623	0.6970	1530
A-1	11562.2	J1-RB	8148	1.7100	1733	0.669	0.7020	1538
A-2-BP	11886.6	J2-RB	6935	1.5716	1399	0.847	0.7264	1236
A-5-BP	12099.2	J2-RB	6299	1.4823	1196	1.041	0.7459	1069
A-4-BP	12300.7	J2-RB	5914	1.4133	1039	1.249	0.7623	941

The tuned 13-component EoS model is applied to the compositions of the other PVT samples (A-3-BP, A-1, A-5-BP, A-4-BP) (Table 2-18). The modeled fluid properties show similar trends to the PVT properties (Figs. 2-15 through 2-20, Tables 2-19, 2-20). Modeled values of bubble point pressure (Figure 2-15), differential GOR (Figure 2-16) formation volume factor (Figure 2-17), density (Figure 2-18), viscosity (Figure 2-19), and multi-stage separator GOR (Figure 2-20) match PVT data well. Simulated density values are consistently higher than PVT data, but deviate by less than 6%.

Modeled values for the A-1 PVT sample (J1-RB reservoir) deviate more than other samples (Figs. 2-15 through 2-20). This is an expected result based on the A-1 PVT reported C_{7+} mole fraction (Figure 2-4, Table 2-2), which does not lie within the gradational trend.

Lumping the 13-Component Model into a 5-Component Model

The 13-component EoS model is "lumped" into a 5-component model to reduce model complexity (Tables 2-21, 2-22). The lumping scheme (Tables 2-23, 2-24) is based on similarity in volatility as presented by Li et al. (1985). Other workers have used similar lumping schemes (Coats, 1985; Wu et al., 1988; Newley et al., 1991). Hong (1982) suggested that a good match between unlumped and lumped phase envelopes indicated that a proper number of pseudo-components were used. The success demonstrated in matching the fluid properties suggests that 5 pseudo-components (Figure 2-21) effectively represent the 13-component system.

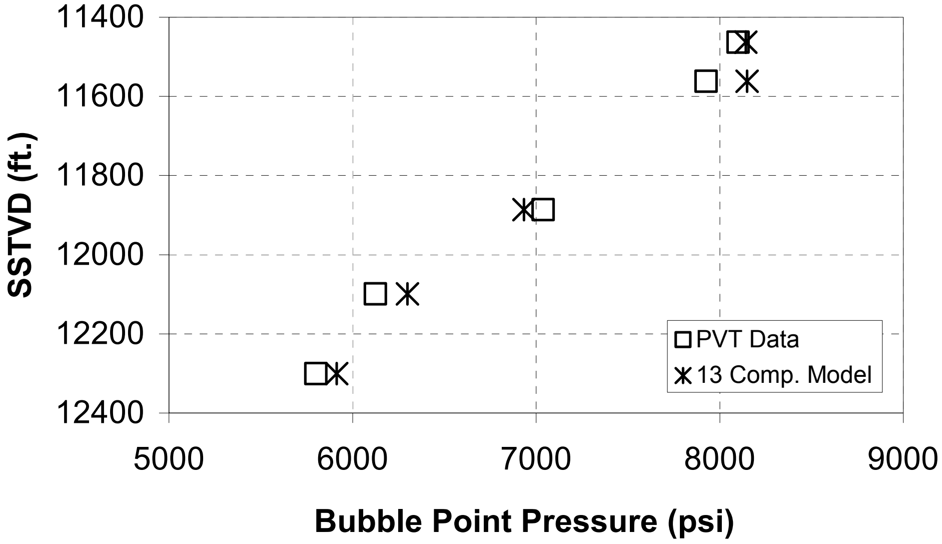

Figure 2-15: Depth versus bubble point pressure comparison for the tuned 13-component model (Tables 2-19, 2-20). Matches are at reservoir temperature (Table 2-1). Data values, from top to bottom, are for the A-3-BP, A-1, A-2-BP, A-5-BP, and A-4-BP sample locations.

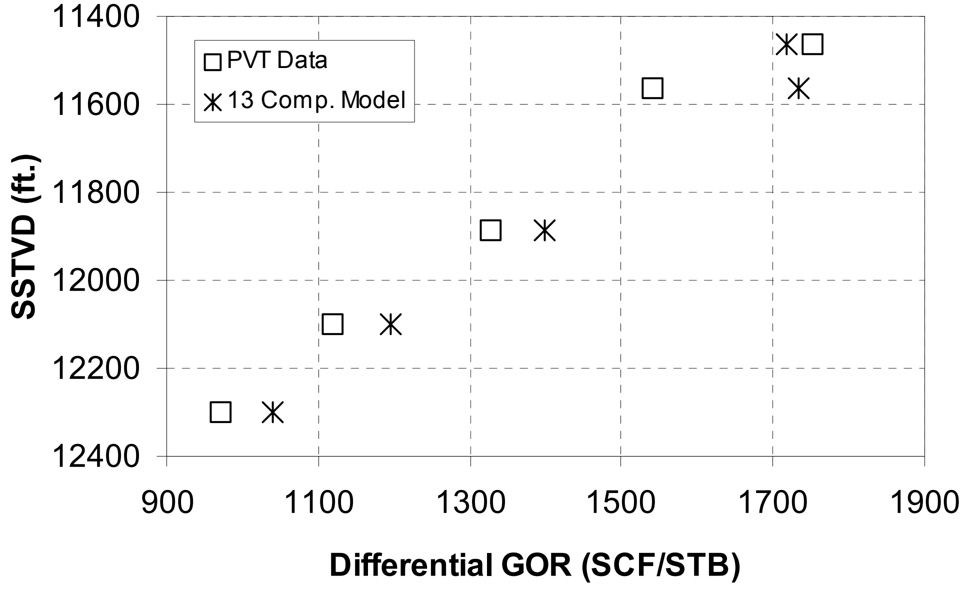

Figure 2-16: Depth versus differential test GOR comparison for the tuned 13-component model (Tables 2-19, 2-20). Matches are at reservoir temperature and pressure (Table 2-1). Data values, from top to bottom, are for the A-3-BP, A-1, A-2-BP, A-5-BP, and A-4-BP sample locations.

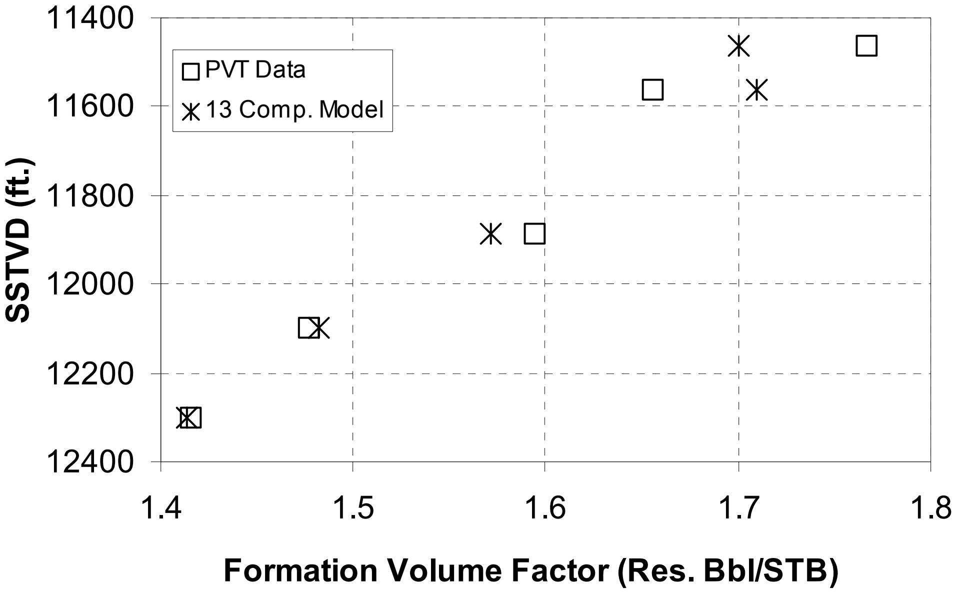

Figure 2-17: Depth versus differential test formation volume factor (*Bo*) comparisons for the tuned 13-component model (Tables 2-19, 2-20). Matches are at reservoir temperature and pressure (Table 2-1). Data values, from top to bottom, are for the A-3-BP, A-1, A-2-BP, A-5-BP, and A-4-BP sample locations.

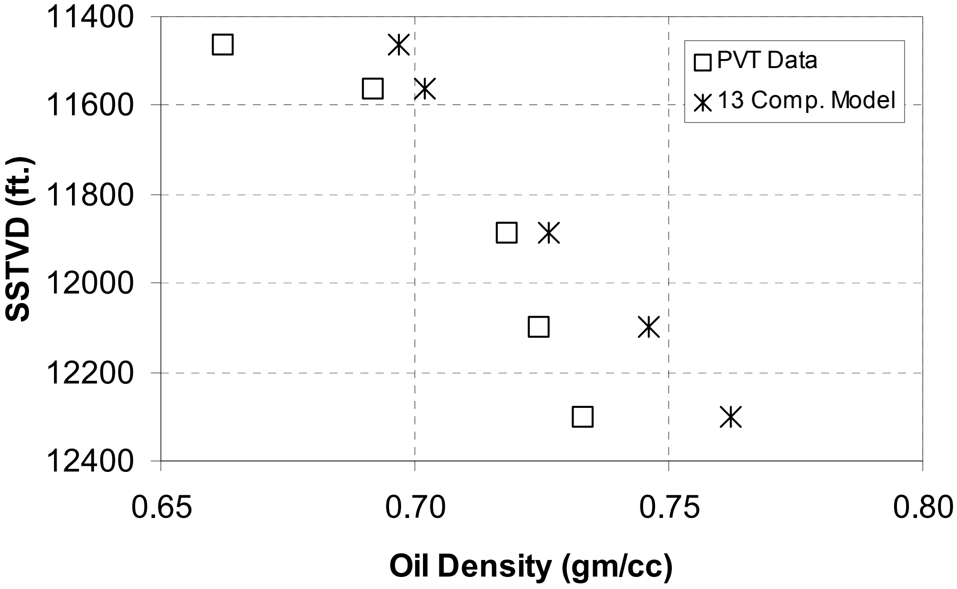

Figure 2-18: Depth versus differential test density comparison for the tuned 13-component model (Tables 2-19, 2-20). Matches are at reservoir temperature and pressure (Table 2-1). Data values, from top to bottom, are for the A-3-BP, A-1, A-2-BP, A-5-BP, and A-4-BP sample locations.

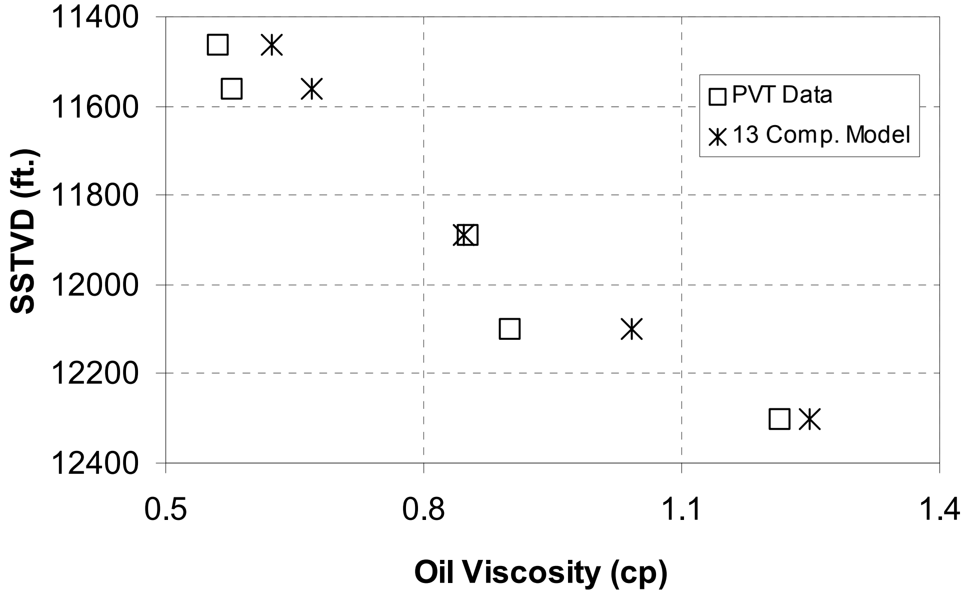

Figure 2-19: Depth versus differential test viscosity comparison for the tuned 13-component model (Tables 2-19, 2-20). Matches are at reservoir temperature and pressure (Table 2-1). Data values, from top to bottom, are for the A-3-BP, A-1, A-2-BP, A-5-BP, and A-4-BP sample locations.

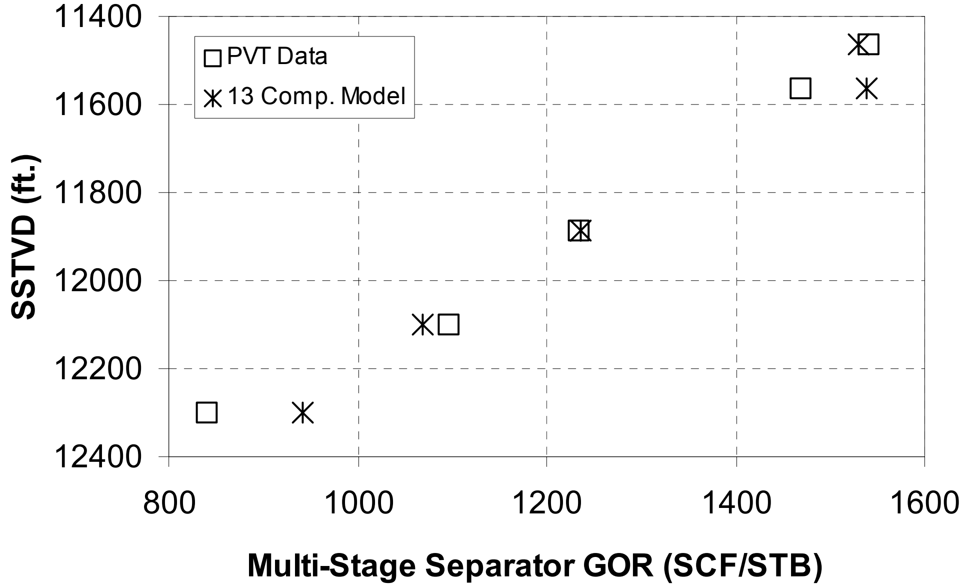

Figure 2-20: Depth versus multi-stage separator GOR comparison for the tuned 13-component model (Tables 2-19, 2-20). Matches are at reservoir temperature and pressure (Table 2-1). Data values, from top to bottom, are for the A-3-BP, A-1, A-2-BP, A-5-BP, and A-4-BP sample locations. The multi-stage separator is a 5 stage separator system (Table 2-10).

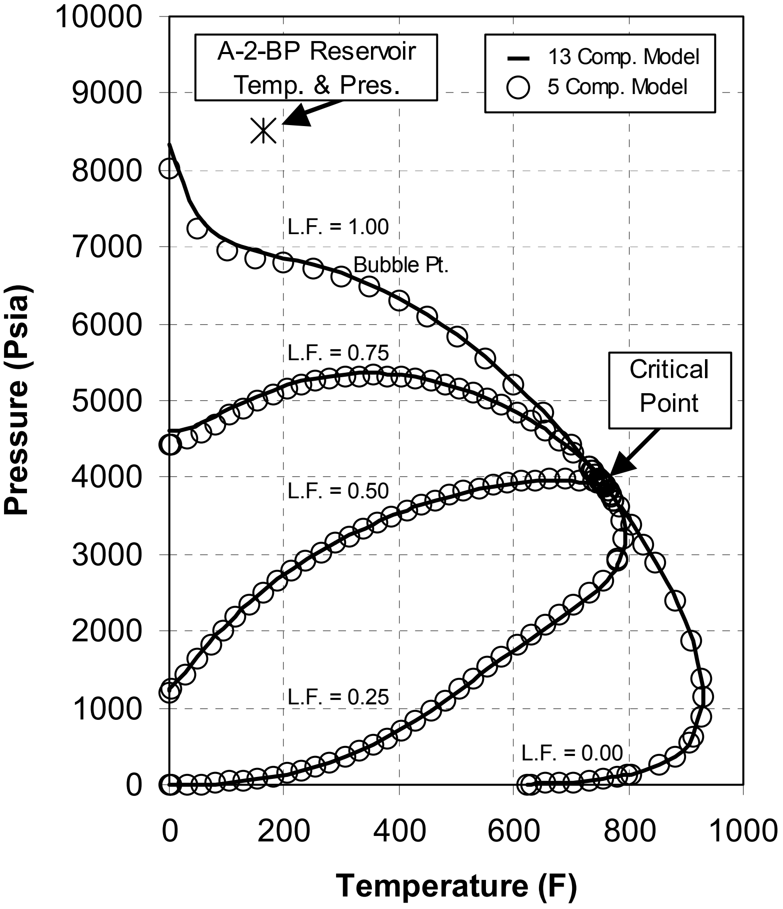

Figure 2-21: Comparison of phase envelopes for the lumped and unlumped A-2-BP fluid models. The phase envelopes and liquid mole fraction (L.F.) quality lines match well. The quality lines are for liquid mole fractions of 1.0 (bubble point), 0.75, 0.50, 0.25, and 0.0. The A-2-BP reservoir temperature (165°F) and pressure (8504 psi) are reported in Table 2-1. The critical point is at 750 °F and 3950 psi

Table 2-21: Lumped 5-component EoS model for the A-2-BP

Name	M.W.	T_c (^oF)	P_c (psi)	Z_c	w	Omega A	Omega B	Parachor	Mole Fraction
C1A	16.06	-116.8	667.5	0.2890	0.0126	0.457062	0.077792	70.9	0.6409
C2_C3	36.62	142.7	671.2	0.2870	0.1250	0.465263	0.078955	128.3	0.0745
C4_C6	72.38	377.0	489.2	0.2728	0.2471	0.467900	0.079071	231.7	0.0676
Hvy1	176.76	752.4	312.3	0.2699	0.5416	0.397167	0.074053	555.5	0.1397
Hvy2	493.72	1359.0	183.8	0.2899	1.2217	0.320202	0.074041	1635.0	0.0773

Table 2-22: Lumped binary interaction parameters for the 5-component model

	C1A	C2_C3	C4_C6	Hvy1
C2_C3	0.00001			
C4_C6	0.02219	0.00993		
Hvy1	0.161365	0.00993	0.0	
Hvy2	0.020191	0.00993	0.0	0.0

Table 2-23: Lumping scheme for EoS model

Lumped Pseudo-Component	Original Components
C1A	$C_1 + N_2$
C2_C3	$C_2 + C_3 + CO_2$
C4_C6	$NC_4 + IC_4 + NC_5 + IC_5 + C_6$
Hvy1	H1 + H2
Hvy2	H3

Table 2-24: Lumped compositions for sample wells

Name	A-3-BP	A-1	A-2-BP	A-5BP	A-4-BP
C1A	0.6740	0.6706	0.6409	0.6172	0.6047
C2_C3	0.0753	0.0757	0.0745	0.0763	0.0688
C4_C6	0.0557	0.0628	0.0676	0.0698	0.0705
Hvy1	0.1345	0.1279	0.1397	0.1457	0.1510
Hvy2	0.0605	0.0630	0.0773	0.0910	0.1050

The fluid properties of the lumped model have the same trends as that of the 13-component model (Figs. 2-22, through 2-27, Tables 2-20, 2-25). Modeled values for the bubble point pressure (Figure 2-22), differential GOR (Figure 2-23) formation volume factor (Figure 2-24), density (Figure 2-25), viscosity (Figure 2-26), and multi-stage separator GOR (Figure 2-27) match well.

Simulated properties deviate more for updip wells (A-1 and A-3-BP) (Figs. 2-22 through 2-27). These deviations are less than 5%, except for the A-1 bubble point pressure (5.7%) (Tables 2-19, 2-25). An increase in the number of pseudo-components can decrease this deviation at a cost of increased computational time.

Adjustment of Fluid Composition to Match Initial Producing GOR

The mole fractions of the 5 pseudo-components are adjusted to match the initial producing GOR (Figs. 2-28, 2-29, 2-30, Tables 2-24, 2-26, 2-27). The adjustments consisted of decreasing the C1A (5%), increasing the Hvy1 (13%), and increasing the Hvy2 (13%) mole fractions (Figs. 2-28, Tables 2-24, 2-26). The Hvy1 and Hvy2 mole fraction values are increased proportionally by weight percent. Larger deviations in GOR (A-5-BP) result in a large adjustment of the methane and the C_{7+} mole fractions (C1A = 4.9%, Hvy1 and Hvy2 = 12.7%). Smaller deviations in GOR (A-1) result in a small adjustment of the methane and the C_{7+} mole fractions (C1A = 0.7%, Hvy1 and Hvy2 = 2.6%).

The adjustment of the mole fractions allow for a match of initial producing GOR but not the remaining PVT fluid properties. The overall effect of this adjustment is a heavier hydrocarbon at all locations than is reported in the PVT data (lower GOR, Psat, Bo, and higher density, viscosity).

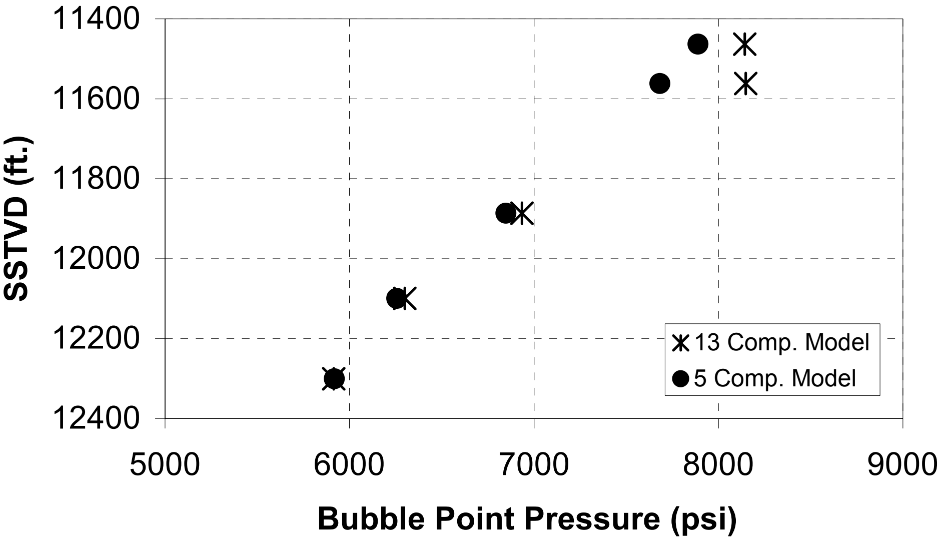

Figure 2-22: Depth versus bubble point pressure for the 5-component and 13-component models (Tables 2-20, 2-25). Comparisons show a good match for the two models. Data values, from top to bottom, are for the A-3-BP, A-1, A-2-BP, A-5-BP, and A-4-BP sample locations.

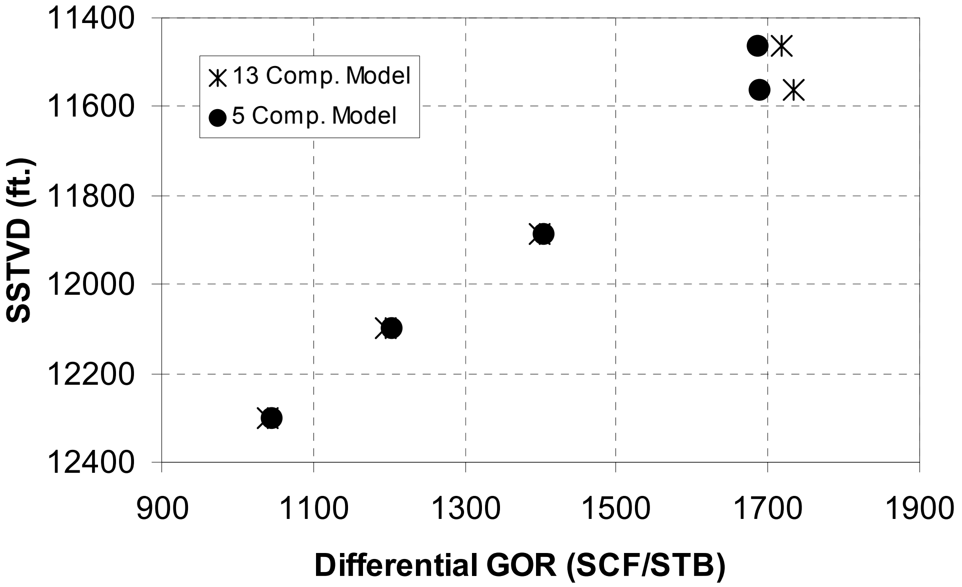

Figure 2-23: Depth versus differential test GOR for the 5-component and 13-component models (Tables 2-20, 2-25). Data values, from top to bottom, are for the A-3-BP, A-1, A-2-BP, A-5-BP, and A-4-BP sample locations.

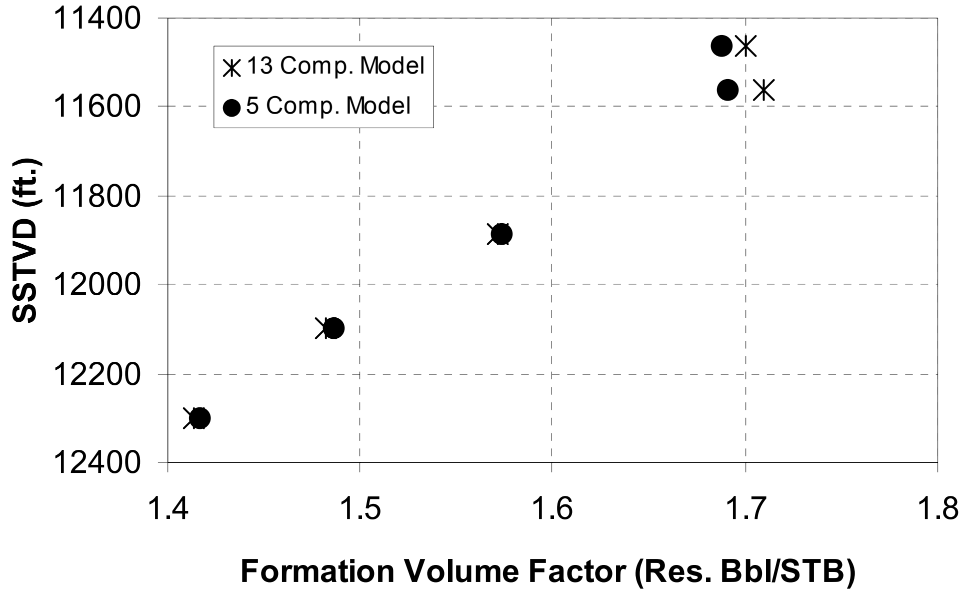

Figure 2-24: Depth versus differential test formation volume factor (*Bo*) for the 5-component and 13-component models (Tables 2-20, 2-25). *Bo* comparisons show a good match for the two models. Data values, from top to bottom, are for the A-3-BP, A-1, A-2-BP, A-5-BP, and A-4-BP sample locations.

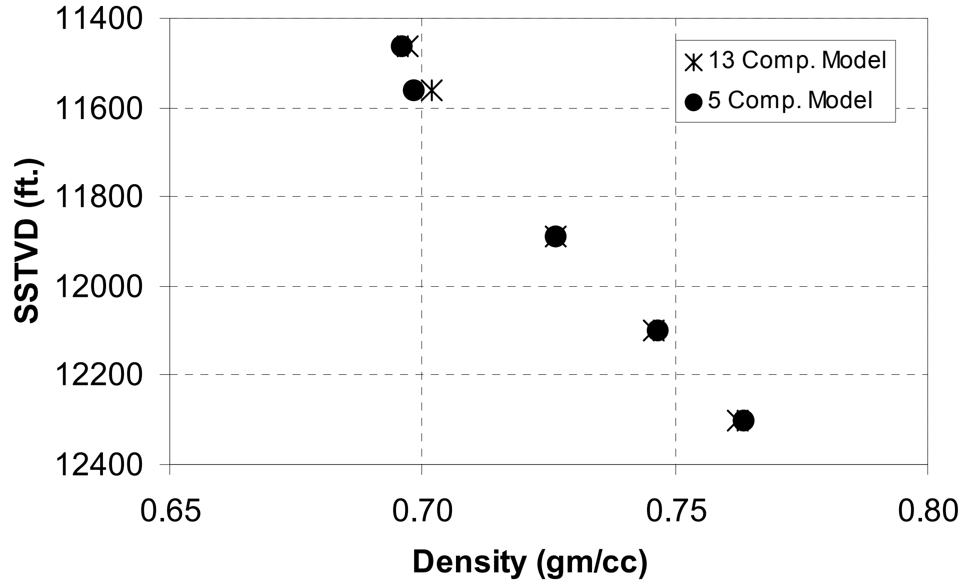

Figure 2-25: Depth versus differential test density for the 5-component and 13-component models (Tables 2-20, 2-25). Density comparisons show a good match for the two models. Data values, from top to bottom, are for the A-3-BP, A-1, A-2-BP, A-5-BP, and A-4-BP sample locations.

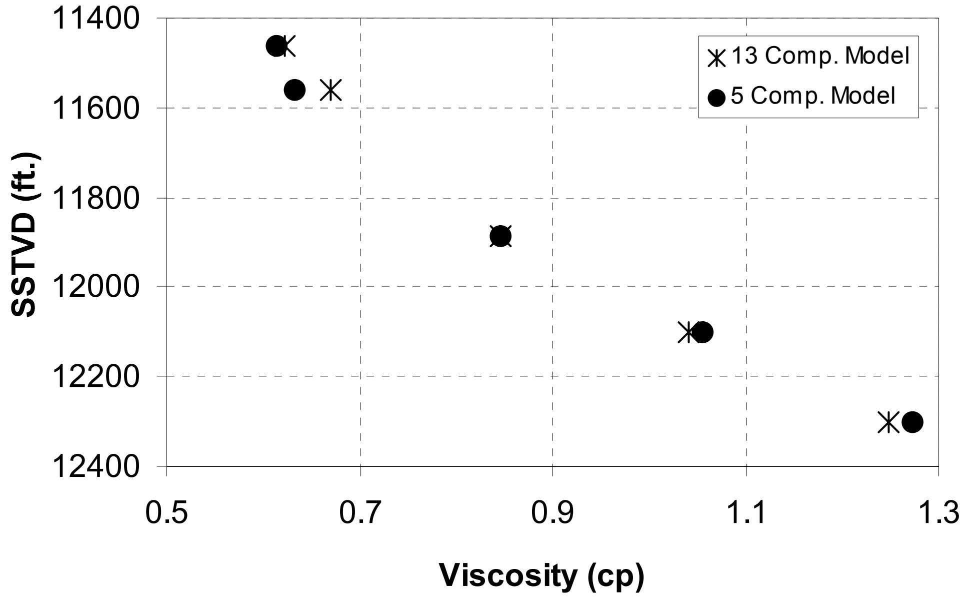

Figure 2-26: Depth versus differential test viscosity for the 5-component and 13-component models (Tables 2-20, 2-25). Viscosity comparisons show a good match for the two models. Data values, from top to bottom, are for the A-3-BP, A-1, A-2-BP, A-5-BP, and A-4-BP PVT sample locations.

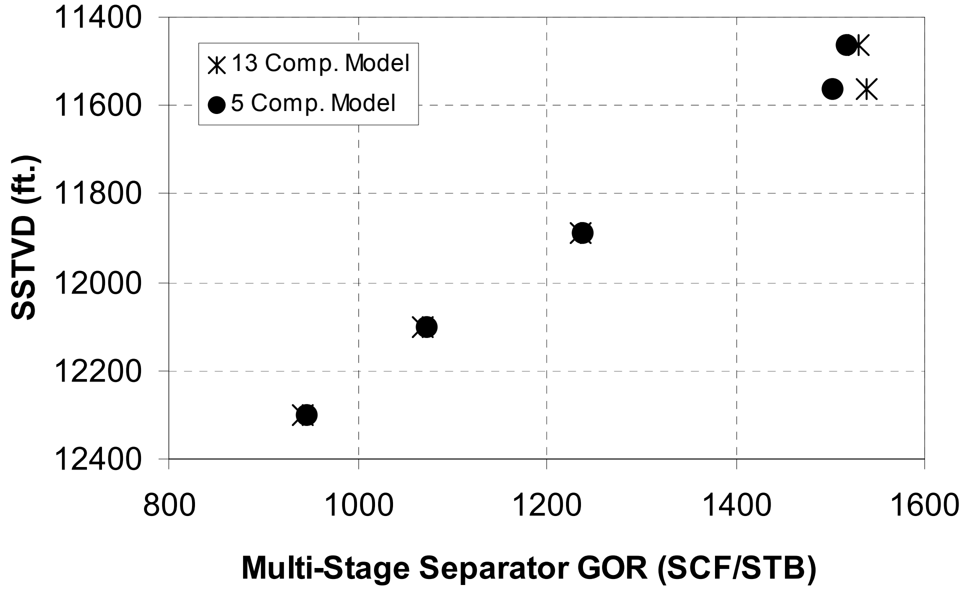

Figure 2-27: Depth versus multi-stage separator GOR for the 5-component and 13-component models (Tables 2-20, 2-25). Data values, from top to bottom, are for the A-3-BP, A-1, A-2-BP, A-5-BP, and A-4-BP PVT sample locations. The multi-stage separator is a 5-stage separator system (Table 2-10).

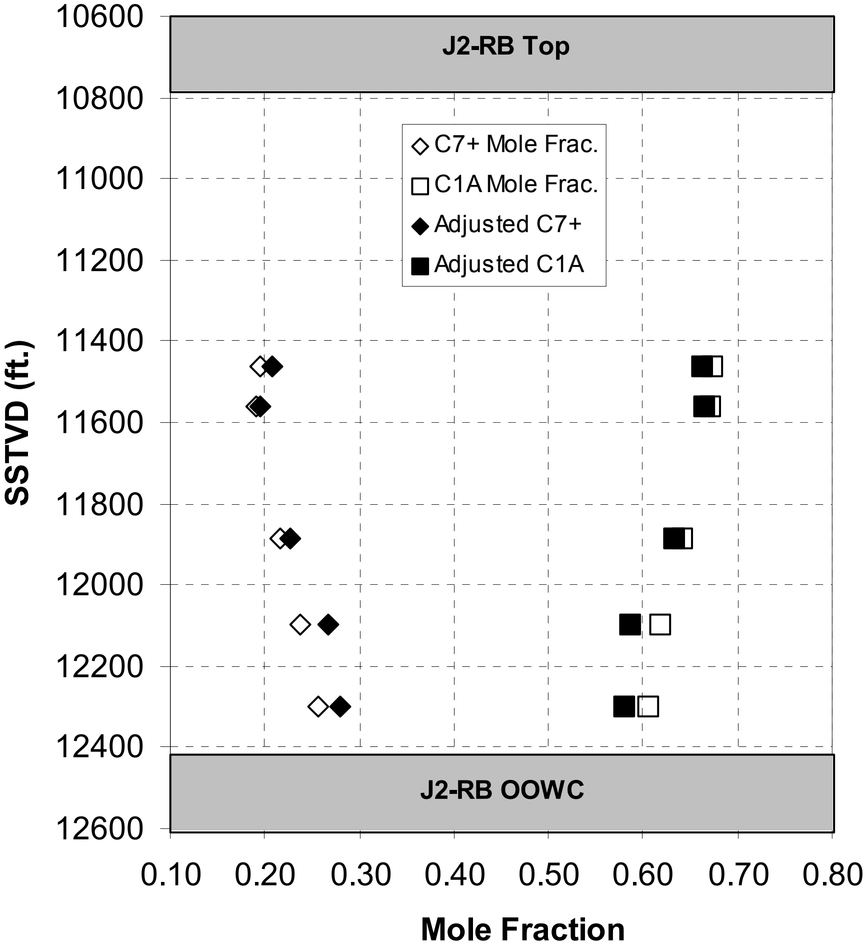

Figure 2-28: C1A and C_{7+} pseudo-component mole fraction versus depth [C_{7+} = Hvy1 + Hvy2] (Tables 2-24, 2-26). Mole fractions are interpreted to be non-representative of the in-situ fluids and are adjusted to match producing GOR. Data values, from top to bottom, are for the A-3-BP, A-1, A-2-BP, A-5-BP, and A-4-BP sample locations.

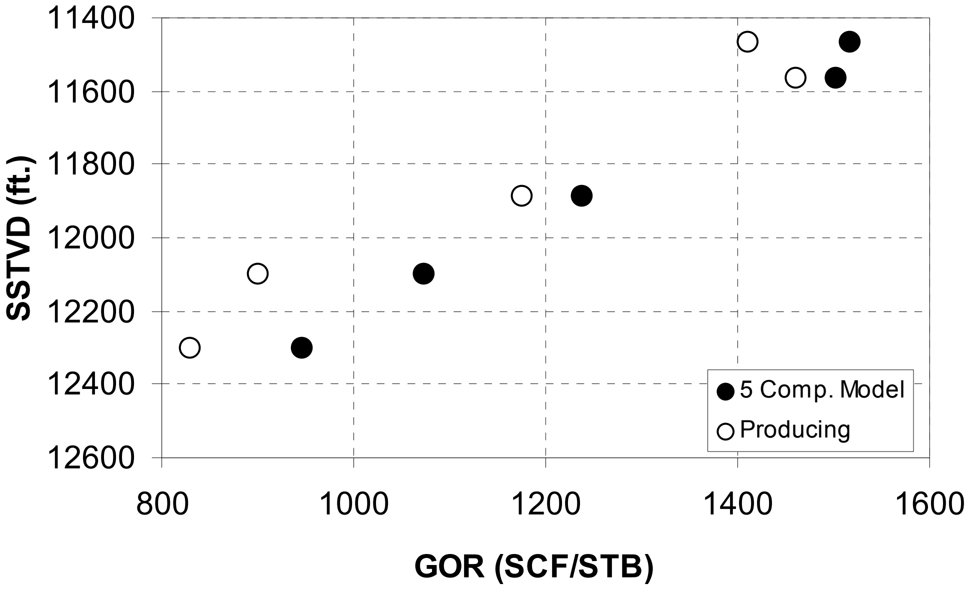

Figure 2-29: Depth versus producing GOR and modeled multi-stage separator GOR (Tables 2-25, 2-27). Data values, from top to bottom, are for the A-3-BP, A-1, A-2-BP, A-5-BP, and A-4-BP sample locations.

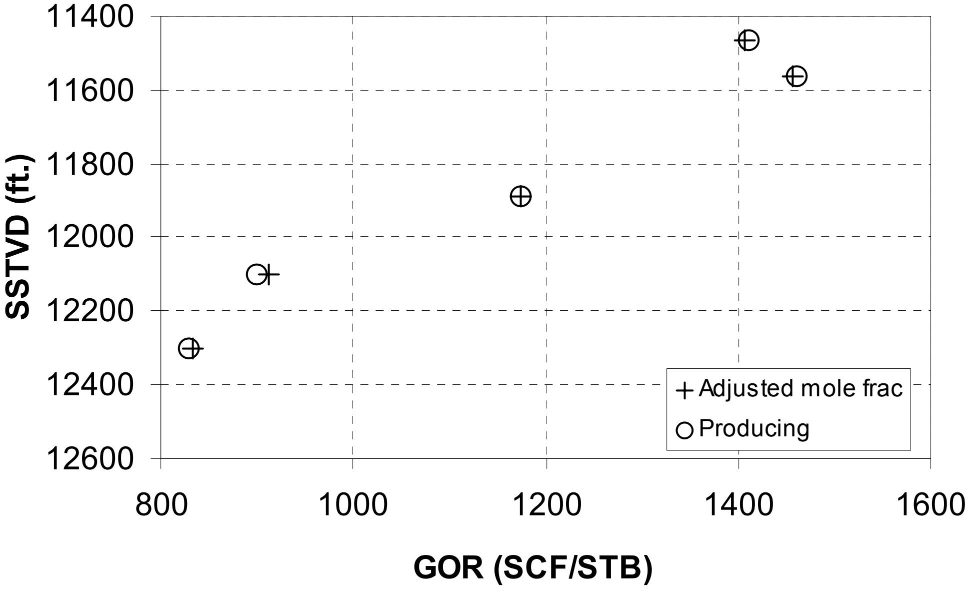

Figure 2-30: Depth versus producing GOR and adjusted mole fraction multi-stage separator GOR (Table 2-27). The mole fractions for the 5-component lumped model are adjusted (Figure 2-28) such that the producing GOR is matched. Large differences in GOR (A-3-BP, A-5-BP, and A-4-BP) result in large changes in C_1 and C_{7+} pseudo-component mole fractions as observed in Figure 2-28. Data values, from top to bottom, are for the A-3-BP, A-1, A-2-BP, A-5-BP, and A-4-BP sample locations.

Table 2-25: Lumped 5-component model fluid properties at reservoir conditions

Well	Depth (ft.)	Reservoir	Bubble Point (psi)	Bo (Res. Bbl/STB)	Differential GOR (SCF/STB)	Viscosity (cp)	Density (gm/cc)	Multi-Stage Separator GOR (SCF/STB)
A-3-BP	11463.4	J2-RB	7890	1.6879	1687	0.614	0.6960	1517
A-1	11562.2	J1-RB	7682	1.6911	1688	0.632	0.6984	1503
A-2-BP	11886.6	J2-RB	6848	1.5735	1405	0.847	0.7264	1237
A-5-BP	12099.2	J2-RB	6257	1.4862	1203	1.056	0.7467	1073
A-4-BP	12300.7	J2-RB	5918	1.4171	1046	1.273	0.7635	946

Table 2-26: Adjusted mole fraction results for producing GOR match

	A-3-BP	A-1	A-2-BP	A-5-BP	A-4-BP
C1A	0.6620	0.6656	0.6319	0.5872	0.5807
C2_C3	0.0753	0.0757	0.0745	0.0763	0.0688
C4_C6	0.0557	0.0628	0.0676	0.0698	0.0705
Hvy1	0.14278	0.13125	0.14544	0.16418	0.16516
Hvy2	0.06422	0.06465	0.08056	0.10252	0.11484

Table 2-27: Comparison of adjusted mole fraction multi-stage separator GOR to producing GOR

Well	Depth (ft.)	Reservoir	Producing GOR (SCF/STB)	Multi-Stage Separator GOR (SCF/STB)
A-3-BP	11463.4	J2-RB	1410	1407.6
A-1	11562.2	J1-RB	1460	1455.9
A-2-BP	11886.6	J2-RB	1175	1173.9
A-5-BP	12099.2	J2-RB	900	913.0
A-4-BP	12300.7	J2-RB	830	834.0

Compositional Equilibrium

The fluids of the J2-RB are not in an equilibrium state (Ratulowski et al., 2000). Hirschberg (1988) stated that the time for fluids, not near the critical conditions, to achieve compositional equilibrium is influenced by asphaltenes. Low diffusion rates of asphaltenes can result in compositional equilibrium times of a few million to a billion years (Hirschberg, 1988).

Work by Bird et al. (1960), and Reerink (1973) is used to estimate the time for compositional equilibrium. Calculations are based on published asphaltene data (molecular weight = 1000 to 10,000 gm/mole, density ~1200 kg/m^3) (Hirschberg, 1988), a vertical reservoir thickness of 1400 ft. at a dip angle of 22^o, reservoir temperature of 165^{o}F, and estimated deasphaltized oil viscosity of 0.4 cp. The time for the J2-RB fluid to reach equilibrium ranges from 7.07 Ma to 15.22 Ma, which is two to three times older than the J-sands (3.35 Ma).

Composition in Depth Scheme

Composition versus Depth

Linear trend lines were fit to the adjusted mole fractions to model the fluid properties for the depth range of the J1 and J2 RB reservoirs (Figs. 2-31 through 2-36, Table 2-28). Further, an extrapolation of mole fractions updip beyond the last known set of mole fractions (A-3-BP) is performed using two methods; (a) along the same linear trend and (Table 2-29) (b) using a constant composition (Table 2-30).

The linear trend lines are fit with a least-squares regression for the C1A (Figure 2-31), C4_C6 (Figure 2-33), Hvy2 (Figure 2-36), and C7+ (Figure 2-34) pseudo-component mole fractions [C7+ = Hvy1 + Hvy2]. Then, the C2_C3 (Figure 2-32) and

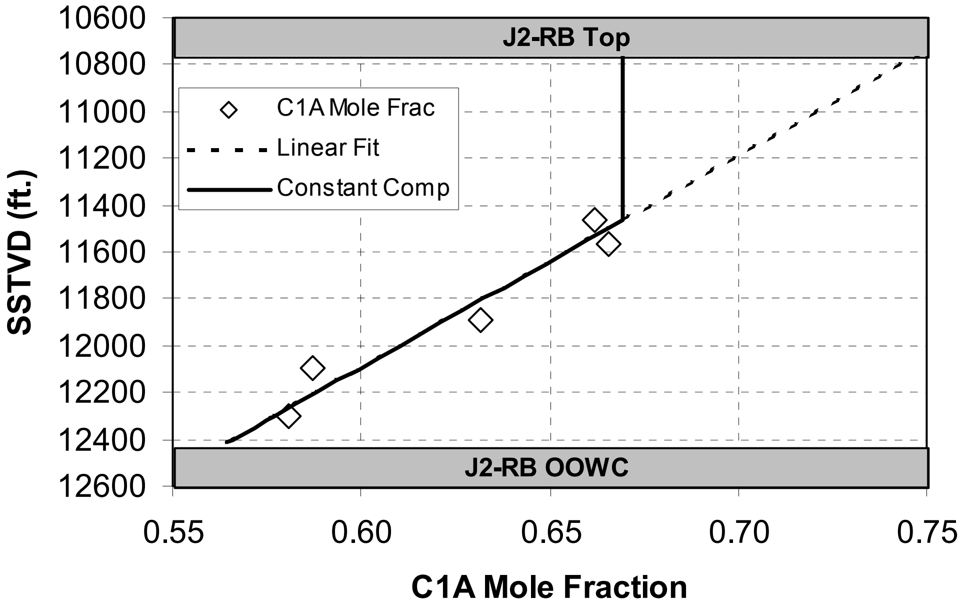

Figure 2-31: Depth versus C1A pseudo-component mole fractions with linear trend fit with a least squares regression. The lumped mole fraction data, from top to bottom, are for the A-3-BP, A-1, A-2-BP, A-5-BP, and A-4-BP sample locations (Table 2-26). Modeled mole fraction data is found in Tables 2-28 and 2-29.

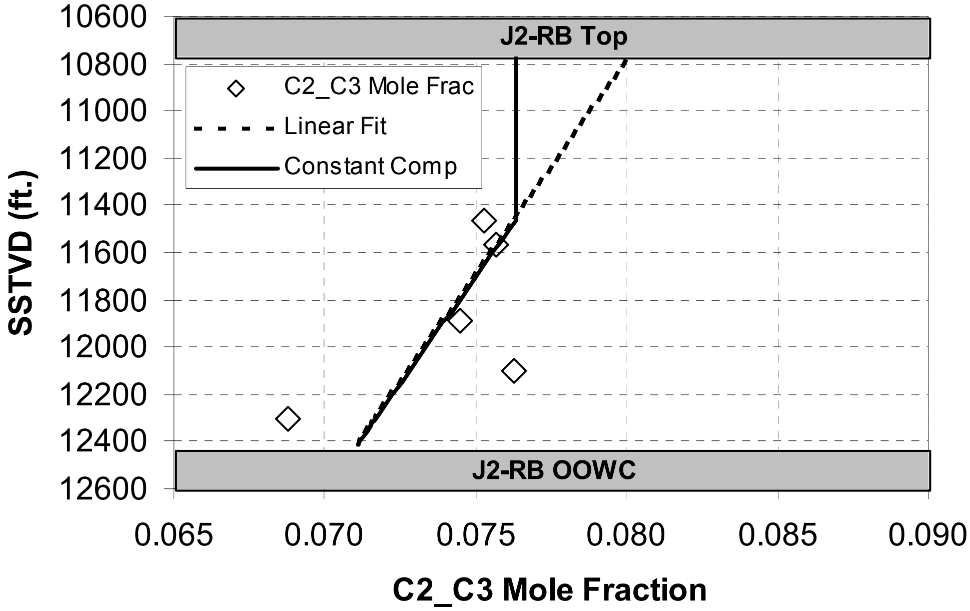

Figure 2-32: Depth versus C2-C3 pseudo-component mole fraction with back-calculated linear trend polynomial. The lumped mole fraction data, from top to bottom, are for the A-3-BP, A-1, A-2-BP, A-5-BP, and A-4-BP sample locations (Table 2-26). The C2-C3 trend curve is calculated based on the sum of the pseudo-components equaling one [$C2\_C3 = 1.0 - (C1A + C4\_C6 + C_{7+})$]. Modeled mole fraction data is found in Tables 2-28 and 2-29.

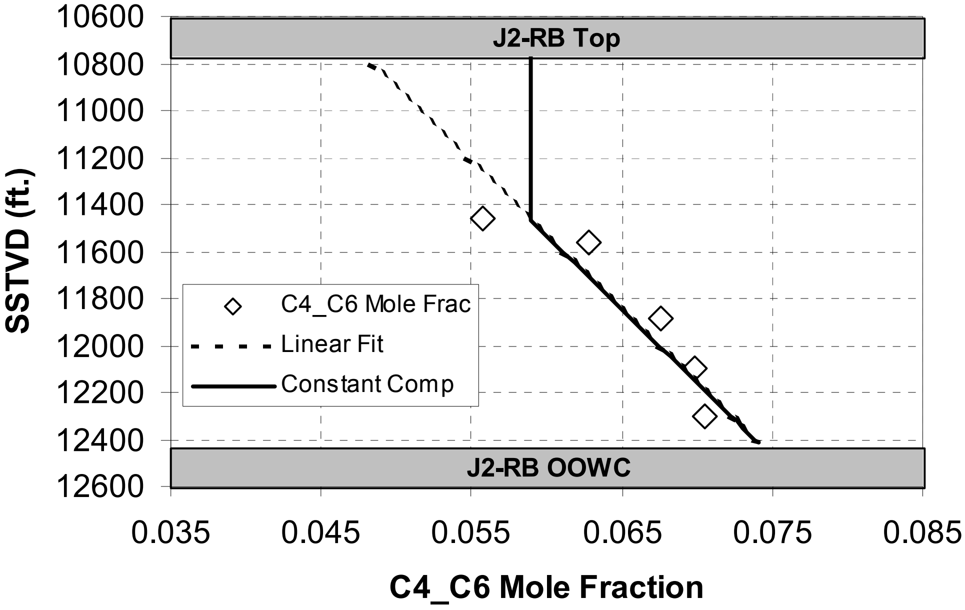

Figure 2-33: Depth versus C4-C6 pseudo-component mole fraction with linear trend fit with a least squares regression. The lumped mole fraction data, from top to bottom, are for the A-3-BP, A-1, A-2-BP, A-5-BP, and A-4-BP sample locations (Table 2-26). Modeled mole fraction data is found in Tables 2-28 and 2-29.

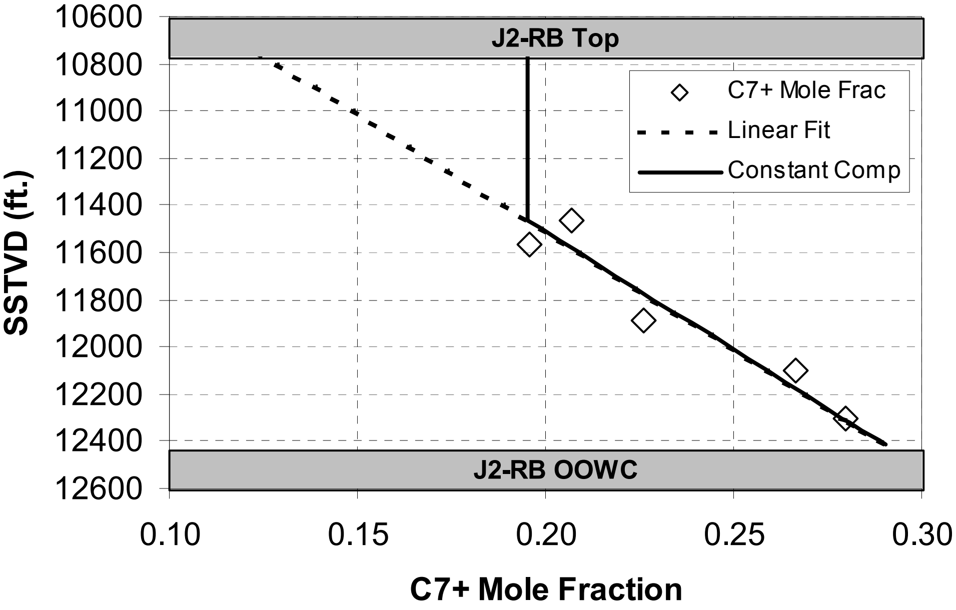

Figure 2-34: Depth versus C_{7+} pseudo-component mole fraction with linear trend fit with a least squares regression. Pseudo-component mole fractions from Hvy1 and Hvy2 were summed to equal the mole fraction of C_{7+} [C_{7+} = Hvy1 + Hvy2]. The lumped mole fraction data, from top to bottom, are for the A-3-BP, A-1, A-2-BP, A-5-BP, and A-4-BP sample locations (Table 2-26). Modeled mole fraction data is found in Tables 2-28 and 2-29.

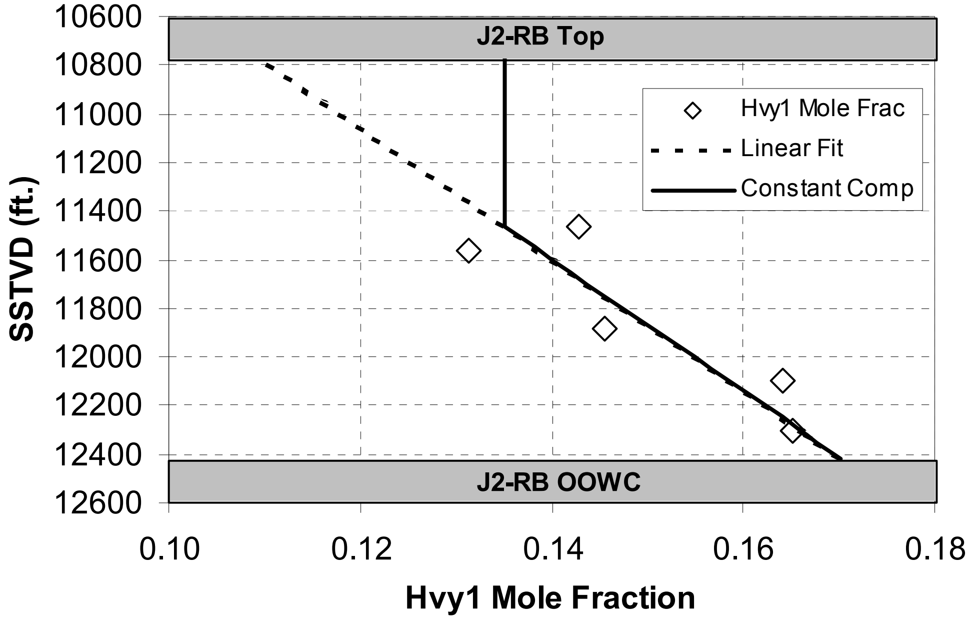

Figure 2-35: Depth versus Hvy1 pseudo-component mole fraction with back-calculated linear trend. The lumped mole fraction data, from top to bottom, are for the A-3-BP, A-1, A-2-BP, A-5-BP, and A-4-BP sample locations (Table 2-26). The Hvy1 trend lines are calculated based on the summation of the Hvy1 and Hvy2 mole fractions equaling the C_{7+} mole fraction [Hvy1 = (C_{7+} - Hvy2)]. Modeled mole fraction data is found in Tables 2-28 and 2-29.

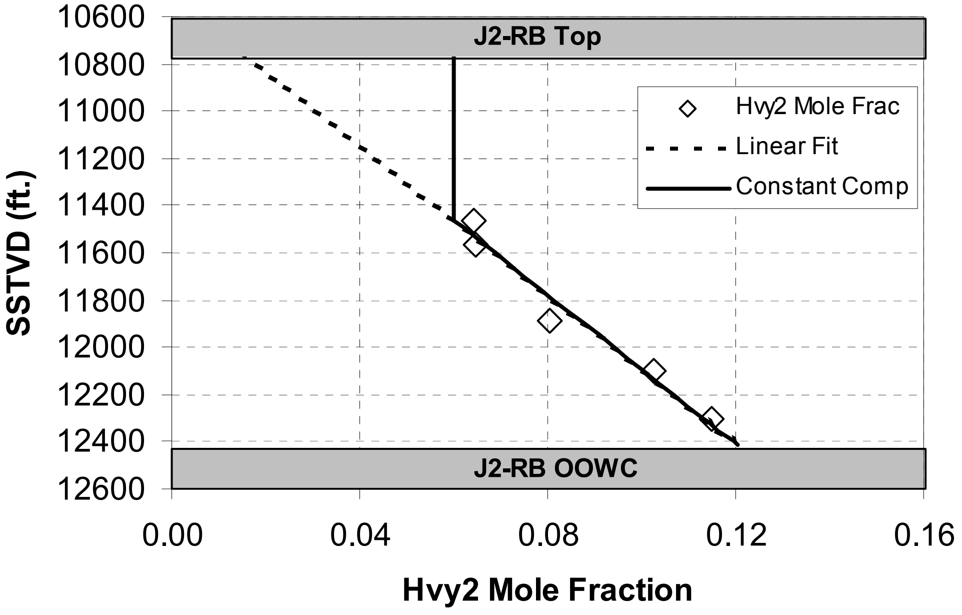

Figure 2-36: Depth versus Hvy2 pseudo-component mole fraction with linear trend fit with a least squares regression. The lumped mole fraction data, from top to bottom, are for the A-3-BP, A-1, A-2-BP, A-5-BP, and A-4-BP sample locations (Table 2-26). Modeled mole fraction data is found in Tables 2-28 and 2-29.

Table 2-28: Linear coefficients for the 5 pseudo-components and C_{7+} mole fractions

i	a_{1i}	a_{2i}
C1A	-1.1073E-04	1.93900
C2_C3	-5.5240E-06	0.13965
C4_C6	1.6024E-05	-0.12480
Hvy1	3.6944E-05	-0.28849
Hvy2	6.3283E-05	-0.66533
C_{7+}	1.0023E-04	-0.95382

Table 2-29: Modeled mole fractions for linear composition extrapolation model.

Depth	C1A	C2_C3	C4_C6	Hvy1	Hvy2
10750	0.74866	0.08027	0.04745	0.10866	0.01496
10800	0.74312	0.07999	0.04826	0.11051	0.01813
10850	0.73758	0.07971	0.04906	0.11235	0.02129
10900	0.73205	0.07944	0.04986	0.11420	0.02445
10950	0.72651	0.07916	0.05066	0.11605	0.02762
11000	0.72097	0.07888	0.05146	0.11789	0.03078
11050	0.71544	0.07861	0.05226	0.11974	0.03395
11100	0.70990	0.07833	0.05306	0.12159	0.03711
11150	0.70436	0.07806	0.05386	0.12344	0.04027
11200	0.69883	0.07778	0.05467	0.12528	0.04344
11250	0.69329	0.07750	0.05547	0.12713	0.04660
11300	0.68776	0.07723	0.05627	0.12898	0.04977
11350	0.68222	0.07695	0.05707	0.13082	0.05293
11400	0.67668	0.07668	0.05787	0.13267	0.05610
11450	0.67115	0.07640	0.05867	0.13452	0.05926
11500	0.66561	0.07612	0.05947	0.13637	0.06242
11550	0.66007	0.07585	0.06027	0.13821	0.06559
11600	0.65454	0.07557	0.06108	0.14006	0.06875
11650	0.64900	0.07529	0.06188	0.14191	0.07192
11700	0.64346	0.07502	0.06268	0.14376	0.07508
11750	0.63793	0.07474	0.06348	0.14560	0.07824
11800	0.63239	0.07447	0.06428	0.14745	0.08141
11850	0.62686	0.07419	0.06508	0.14930	0.08457
11900	0.62132	0.07391	0.06588	0.15114	0.08774
11950	0.61578	0.07364	0.06668	0.15299	0.09090
12000	0.61025	0.07336	0.06748	0.15484	0.09406
12050	0.60471	0.07308	0.06829	0.15669	0.09723
12100	0.59917	0.07281	0.06909	0.15853	0.10039
12150	0.59364	0.07253	0.06989	0.16038	0.10356
12200	0.58810	0.07226	0.07069	0.16223	0.10672
12250	0.58256	0.07198	0.07149	0.16407	0.10989
12300	0.57703	0.07170	0.07229	0.16592	0.11305
12320	0.57481	0.07159	0.07261	0.16666	0.11432
12350	0.57149	0.07143	0.07309	0.16777	0.11621
12400	0.56596	0.07115	0.07389	0.16962	0.11938
12415	0.56429	0.07107	0.07413	0.17017	0.12033

Table 2-30: Modeled mole fractions for constant composition extrapolation model. Bold values are mole fractions for the A-3-BP.

Depth	C1A	C2_C3	C4_C6	Hvy1	Hvy2
10750	0.66949	0.07632	0.05891	0.13507	0.06021
10800	0.66949	0.07632	0.05891	0.13507	0.06021
10850	0.66949	0.07632	0.05891	0.13507	0.06021
10900	0.66949	0.07632	0.05891	0.13507	0.06021
10950	0.66949	0.07632	0.05891	0.13507	0.06021
11000	0.66949	0.07632	0.05891	0.13507	0.06021
11050	0.66949	0.07632	0.05891	0.13507	0.06021
11100	0.66949	0.07632	0.05891	0.13507	0.06021
11150	0.66949	0.07632	0.05891	0.13507	0.06021
11200	0.66949	0.07632	0.05891	0.13507	0.06021
11250	0.66949	0.07632	0.05891	0.13507	0.06021
11300	0.66949	0.07632	0.05891	0.13507	0.06021
11350	0.66949	0.07632	0.05891	0.13507	0.06021
11400	0.66949	0.07632	0.05891	0.13507	0.06021
11465	**0.66949**	**0.07632**	**0.05891**	**0.13507**	**0.06021**
11500	0.66561	0.07612	0.05947	0.13637	0.06242
11550	0.66007	0.07585	0.06027	0.13821	0.06559
11600	0.65454	0.07557	0.06108	0.14006	0.06875
11650	0.64900	0.07529	0.06188	0.14191	0.07192
11700	0.64346	0.07502	0.06268	0.14376	0.07508
11750	0.63793	0.07474	0.06348	0.14560	0.07824
11800	0.63239	0.07447	0.06428	0.14745	0.08141
11850	0.62686	0.07419	0.06508	0.14930	0.08457
11900	0.62132	0.07391	0.06588	0.15114	0.08774
11950	0.61578	0.07364	0.06668	0.15299	0.09090
12000	0.61025	0.07336	0.06748	0.15484	0.09406
12050	0.60471	0.07308	0.06829	0.15669	0.09723
12100	0.59917	0.07281	0.06909	0.15853	0.10039
12150	0.59364	0.07253	0.06989	0.16038	0.10356
12200	0.58810	0.07226	0.07069	0.16223	0.10672
12250	0.58256	0.07198	0.07149	0.16407	0.10989
12300	0.57703	0.07170	0.07229	0.16592	0.11305
12320	0.57481	0.07159	0.07261	0.16666	0.11432
12350	0.57149	0.07143	0.07309	0.16777	0.11621
12400	0.56596	0.07115	0.07389	0.16962	0.11938
12415	0.56429	0.07107	0.07413	0.17017	0.12033

Hvy1 (Figure 2-35) pseudo-component mole fractions are calculated; [C2_C3 = 1.0 – (C1A + C4_C6 + C7+)] and [Hvy1 = (C7+) - Hvy2].

The mole fraction (*n*) for each pseudo-component '*i*' for depth (z) is defined by a linear polynomial (Equations 2-1) (Tables 2-29, and 2-30).

$$n_i = a_{1i} z + a_{2i} \tag{2-1}$$

where 'n_i' is the mole fraction of the ith component, 'a_{1i}, a_{2i}' are the coefficients of the ith component (Table 2-28), and '*z*' is depth in feet (positive).

Results - Property Comparison

The fluid properties, for the J1 and J2 RB reservoirs are predicted, using the two mole fraction extrapolation models (Figs. 2-37 through 2-41, Tables 2-31, 2-32). The fluid properties from the two models are the same for the known data range, and deviate, updip, beyond the last known PVT sample (A-3-BP). An initial two-phase region is predicted for the linear mole fraction extrapolation model above 11300 ft., SSTVD. The constant composition extrapolation model predicts the undersaturated condition for all depth. Both models predict the producing GOR for the known data range well, as expected.

These results describe two initial fluid conditions that may exist in the J1 and J2 RB reservoirs. These fluid models are used as inputs for simulation to determine the best mole fraction model.

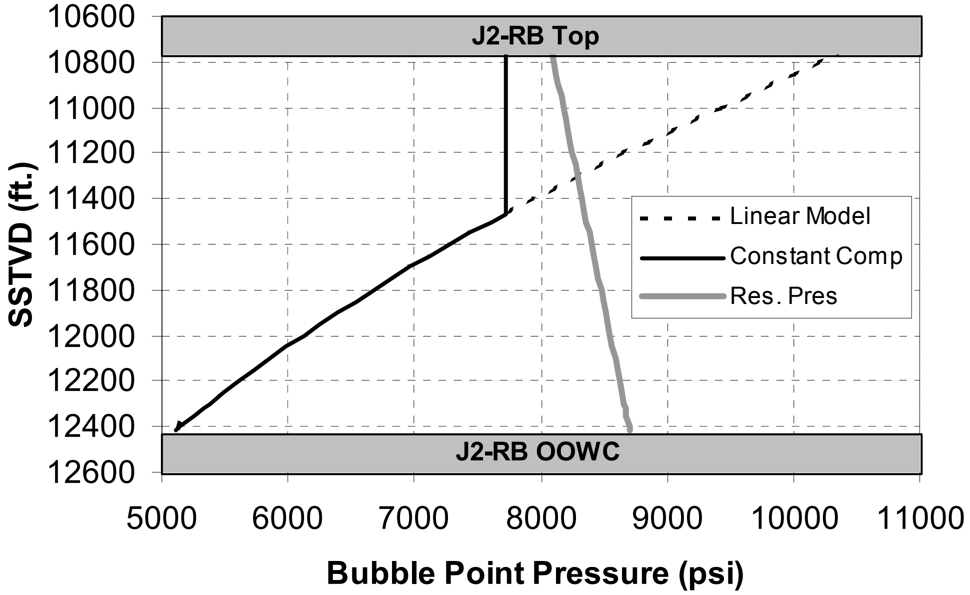

Figure 2-37: Depth vs. modeled bubble point pressure for both linear and constant mole fraction extrapolations (Tables 2-30, 2-31). The linear extrapolation model predicts the presence of an updip two-phase region (above the point where the reservoir pressure intersects the saturation pressure) while the constant composition extrapolation designated the reservoir as entirely undersaturated.

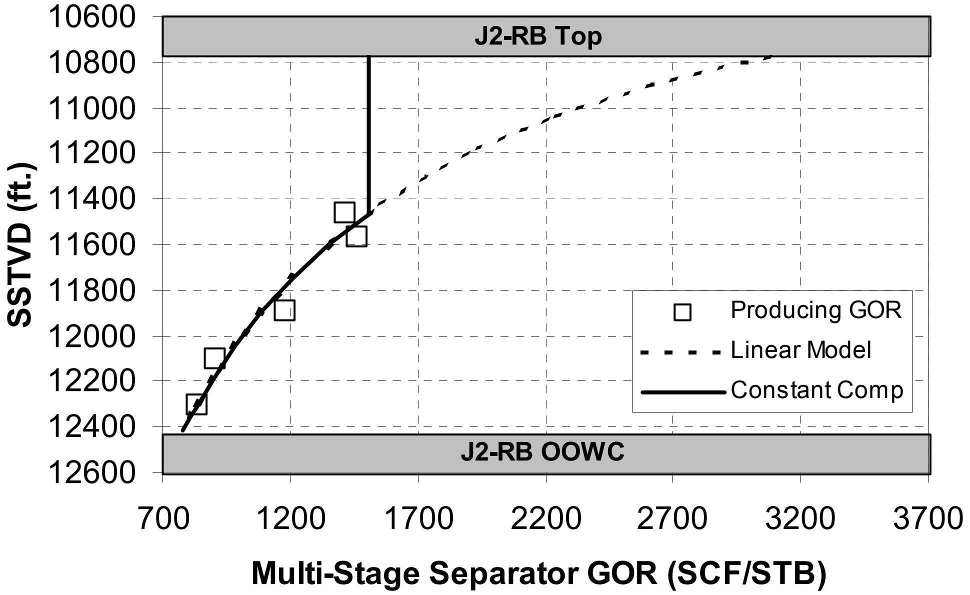

Figure 2-38: Depth vs. modeled multi-stage separator GOR for both linear and constant mole fraction extrapolations (Tables 2-30, 2-31). Both models predict producing GOR well within the region of well data. Producing GOR data, from top to bottom, are for the A-3-BP, A-1, A-2-BP, A-5-BP, and A-4-BP sample locations (Table 2-5).

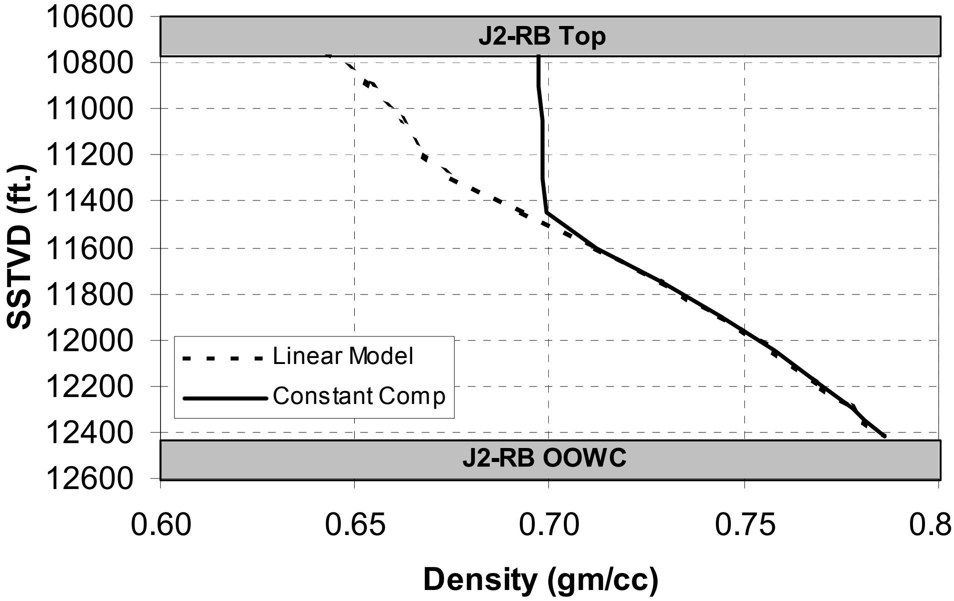

Figure 2-39: Depth vs. modeled density for both linear and constant mole fraction extrapolations (Tables 2-30, 2-31).

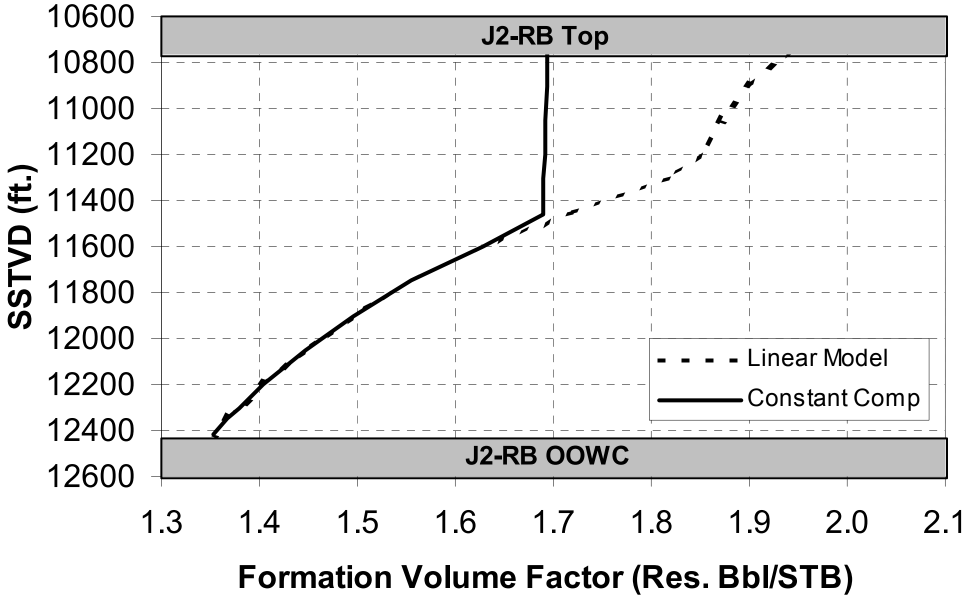

Figure 2-40: Depth vs. modeled formation volume factor (*Bo*) for both linear and constant mole fraction extrapolations (Tables 2-30, 2-31).

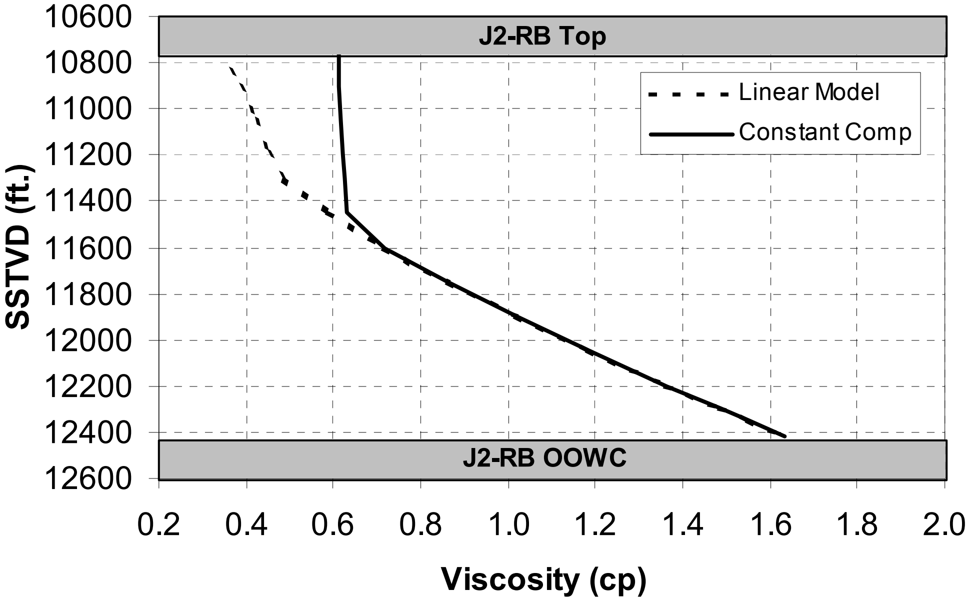

Figure 2-41: Depth vs. modeled viscosity for both linear and constant mole fraction extrapolations (Tables 2-30, 2-31).

Table 2-31: Modeled fluid properties for the linear composition extrapolation model

Depth (ft.)	Reservoir Pressure (psi)	Bubble Point Pressure (psi)	Multi-Stage Separator GOR (SCF/STB)	Bo (Res. Bbl/STB)	Density (gm/cc)	Viscosity (cp)
10750	8085.0	10402.0	3179.1	1.942	0.643	0.341
10900	8140.8	9835.4	2618.6	1.9	0.654	0.387
11050	8196.6	9242.2	2211	1.872	0.662	0.423
11200	8252.4	8665.0	1901.4	1.851	0.668	0.454
11300	8289.6	8295.0	1733.1	1.818	0.675	0.489
11450	8345.4	7769.0	1522.9	1.721	0.693	0.588
11600	8401.2	7277.0	1350.9	1.629	0.712	0.718
11750	8457.0	6817.0	1207.6	1.556	0.729	0.863
11900	8512.8	6387.0	1086.2	1.496	0.744	1.019
12050	8568.6	5986.0	982.2	1.446	0.758	1.186
12200	8624.4	5611.0	892.1	1.404	0.77	1.363
12300	8661.6	5374.9	838.4	1.379	0.778	1.486
12350	8680.2	5260.8	813.3	1.368	0.781	1.549
12415	8704.4	5115.9	782.1	1.353	0.786	1.632

Table 2-32: Modeled fluid properties for the constant composition extrapolation model

Depth (ft.)	Reservoir Pressure (psi)	Bubble Point Pressure (psi)	Mulit-Stage Separator GOR (SCF/STB)	Bo (Res. Bbl/STB)	Density (gm/cc)	Viscosity (cp)
10750	8085.0	7718.6	1504.2	1.694	0.697	0.61
10900	8140.8	7718.6	1504.2	1.693	0.697	0.614
11050	8196.6	7718.6	1504.2	1.692	0.698	0.618
11200	8252.4	7718.6	1504.2	1.691	0.698	0.622
11300	8289.6	7718.6	1504.2	1.69	0.698	0.626
11465	8351.0	7718.6	1504.2	1.689	0.699	0.629
11600	8401.2	7277.0	1350.9	1.629	0.712	0.718
11750	8457.0	6817.0	1207.6	1.556	0.729	0.863
11900	8512.8	6387.0	1086.2	1.496	0.744	1.019
12050	8568.6	5986.0	982.2	1.446	0.758	1.186
12200	8624.4	5611.0	892.1	1.404	0.77	1.363
12300	8661.6	5374.9	838.4	1.379	0.778	1.486
12350	8680.2	5260.8	813.3	1.368	0.781	1.549
12415	8704.4	5115.9	782.1	1.353	0.786	1.632

Conclusions

A compositional fluid model was constructed to establish original fluids in place and model fluid dynamics for reservoir simulation of the J1 and J2 sands. Vertical variations in GOR and saturation pressure are the basis for use of a compositional model.

The J-sand fluids are characterized. The J2-RB fluid samples show a consistent trend in composition and fluid properties and are in pressure communication. Based on these observations the J2-RB fluids are interpreted to represent a compositionally graded reservoir. Composition and fluid properties from a sample in the J1-RB lie within the same trends as the J2-RB and are interpreted to be similar. The variation in composition with depth is assumed to be due to gravitational segregation.

The J3 and J4 reservoir fluids are different based on fluid properties, compositions, and production data.

An Equation of State fluid model is constructed based on middip PVT sample fluid properties from the J2-RB. Use of a mid-dip sample assumes that the sample is an average representative sample.

Methane and C_{7+} mole fractions are adjusted to account for differences between producing GOR and PVT sample separator GOR, thus creating a heavier fluid than is recorded in the PVT data. Based on this the PVT sample properties are interpreted to be non-representative of the in-situ fluids.

Adjusted mole fractions are fitted with a linear trend in the known data range and extrapolated in two extreme fashions to enable fluid property predictions for all depth. Both models are used to determine a mole fraction in depth model that best describe the in-situ fluids and fluid behavior through time.